KLC4 shapes axon arbors during development and mediates adult behavior

Elizabeth M. Haynes[1,2,3], Jiaye "Henry" He[4,5], Marcel Jean-Pierre[1,3], Martin Jarzyna[1,3], Kevin W. Eliceiri[2,4], Jan Huisken[1,4], and Mary C. Halloran[1,3]

1.Department of Integrative Biology, University of Wisconsin-Madison

2. Center for Quantitative Cell Imaging, University of Wisconsin-Madison

3. Department of Neuroscience, University of Wisconsin-Madison

4. Morgridge Institute for Research, Madison, WI

5. National Innovation Center for Advanced Medical Devices, Shenzen, China.

*Corresponding author:
Mary C. Halloran
Department of Integrative Biology
1117 W. Johnson Street
Madison, WI 53706
mchalloran@wisc.edu
608-263-7875

Abstract

Development of elaborate and polarized neuronal morphology requires precisely regulated transport of cellular cargos by motor proteins such as kinesin-1. Kinesin-1 has numerous cellular cargos which must be delivered to unique neuronal compartments. The process by which this motor selectively transports and delivers cargo to regulate neuronal morphogenesis is poorly understood. Our work implicates one kinesin light chain subunit, KLC4, as an essential regulator of axon branching and arborization pattern of sensory neurons during development. Using several live imaging approaches in *klc4* mutant zebrafish, we show that KLC4 is required for stabilization of nascent axon branches and for proper microtubule (MT) dynamics. Furthermore, KLC4 is required for the contact repulsion necessary for tiling of peripheral axon arbors: in *klc4* mutants, peripheral axons showed abnormal fasciculation, a behavior characteristic of central axons, suggesting that KLC4 patterns axonal compartments and helps define axon identity. Finally, we find that *klc4* mutant adults show anxiety-like behavior in a novel tank test, implicating *klc4* as a novel gene involved in stress response circuits.

Introduction

Proper development of complex neuronal morphology and assembly of neural circuits requires tight regulation of axon growth and branching. Precise control over axon branch formation is essential not only for development but also for plasticity and regeneration after injury. Branching allows one neuron to innervate numerous targets, and in many cases, neurons extend multiple axons or branches that navigate to distinct targets. Many molecular signaling pathways can influence branching (Gallo, 2011; Kalil and Dent, 2014), although the mechanisms that control branch formation are still not fully understood. Vertebrate sensory neurons, including Rohon-Beard (RB) neurons, serve as an ideal model to study mechanisms of branching and neuronal morphogenesis. Sensory neurons must extend separate axon branches to targets in the periphery and to the CNS to relay sensory information. Peripheral and central axons have different capacity for branching (Andersen et al., 2011), and behave differently when contacting other axons—central axons fasciculate with one another while peripheral axons show contact repulsion (Liu and Halloran, 2005; Sagasti et al., 2005). Contact repulsion of peripheral axons is necessary for establishment of proper axon arbor patterns that “tile” with arbors from other neurons to effectively innervate the sensory field. Despite the importance of establishing axons with distinct character and branching patterns, the mechanisms regulating molecular compartmentalization of separate axons from one neuron are poorly understood.

Molecular compartmentalization of neurons depends on precisely controlled transport of vesicle and organelle cargos to specific cell locations. Cargos are transported by motor proteins that move in a directional manner along microtubule (MT) tracks. Kinesin-1, the founding member of the kinesin superfamily of motor proteins, is a heterotetramer composed of homodimers of kinesin heavy chains (KHCs), which contain the MT binding and ATPase motor domains, and of kinesin light chains (KLCs), which interact with cargos. Kinesin-1 can mediate long-distance, anterograde transport of multiple cargos including mitochondria, synaptic vesicle precursors, endosomes, lysosomes and RNA granules (Hirokawa et al., 2010; Morfini et al., 2016). Kinesin-1 also has roles in organizing MT tracks. The forces it exerts can physically influence the MT lattice (Shima et al., 2018; Triclin et al., 2021). It can also cross-link MTs by combined interactions of the motor domain and a second MT binding site in the KHC tail, and slide MTs along one another, thereby influencing cell shape (Lu and Gelfand, 2017). While it is clear that kinesin-1 is essential for proper development of the nervous system, the mechanisms by

which it achieves cell-context specificity of its multiple functions and how its cargo-binding and MT-organizing functions are regulated have yet to be fully defined.

The specific activities of kinesin-1 in a given context are likely governed in part by KLCs. KLCs are known to mediate binding between the kinesin motor and cellular cargos, and also to activate the motor by releasing KHC autoinhibition (Morfini et al., 2016; Wong et al., 2010; Wozniak and Allan, 2006). Vertebrates have four *klc* genes (*klc1-4*), with *klc1, 2* and *4* expressed in the nervous system, but our knowledge of the different roles played by individual KLCs in neurons remains very limited. In *Drosophila*, mutants for the single *klc* gene are lethal in larval stages and have defects in neural development (Gindhart et al., 1998; Mochizuki et al., 2011), indicating essential neural functions for KLC. Growing evidence supports the idea that molecular functions are divided among vertebrate KLCs and that each has unique roles. Structural and biochemical studies show that KLC1 and KLC2 have differing affinities for cargo adaptor proteins such as JIP1 and JIP3 (Cockburn et al., 2018; Pernigo et al., 2018; Zhu et al., 2012). Research to date has begun to define distinct neurophysiological functions of KLC1 and KLC2. Studies of mouse *klc1* mutants revealed functions for KLC1 in regulating motor behavior (Rahman et al., 1999), transport of amyloid precursor protein into axons (Kamal et al., 2000), phagosome transport in retinal pigment epithelium (Jiang et al., 2015), and axon guidance and cannabinoid recepter transport during neural development (Saez et al., 2020). A study using a peptide inhibitor of KLC2 phosphorylation showed that KLC2 regulates synaptic plasticity, AMPAR trafficking and mood associated behavior (Du et al., 2010). Mutations in human *klc2* cause SPOAN syndrome, which is characterized by progressive Spastic Paraplegia, Optic Atrophy and Neuropathy, with onset in infancy (Bazvand et al., 2021; Melo et al., 2015). On the whole, previous work supports the idea that individual KLCs have unique, indispensable functions, but has only begun to reveal the specific cellular functions for individual KLCs.

In contrast to KLC1 and KLC2, KLC4 has been the subject of few studies. Mutation of *KLC4* in humans causes a type of hereditary spastic paraplegia (HSP) that manifests in early childhood (Bayrakli et al., 2015), indicating essential developmental functions. To date, the only cellular function shown for KLC4 is that it supports mitochondrial function and confers resistance to radiation in cancer cells (Baek et al., 2018). A clear cellular function for KLC4 in neurons and therefore insight into the *KLC4* mutation-related pathology is lacking.

In this study, we reveal critical functions for KLC4 in sensory axon branching and compartmentalization during development, and in regulation of adult animal behavior. Using live imaging in *klc4* mutant zebrafish, we found that KLC4 is required for peripheral sensory axon branching and proper arborization pattern. This branching defect does not reflect a general growth defect, as axons grew faster in *klc4* mutants and did not show signs of degeneration. Live imaging also showed that *klc4* mutant peripheral axons have defects in contact repulsion and instead often fasciculate with one another, a behavior characteristic of central axons, suggesting KLC4 may contribute to the molecular compartmentalization that defines differential behavior of these axons. Using high-speed, *in vivo* imaging of MT dynamics we showed that *klc4* mutant axons have altered MT dynamics. Finally, we investigated the ramifications of KLC4 loss on adult animal behavior. We found that *klc4* mutant adults exhibit increased anxiety-like behavior, indicating essential roles for KLC4 in neural circuit formation and/or function in adults.

Results

klc4 is expressed during early development

klc genes encode proteins with conserved functional domains including the heptad repeat region that mediates binding to KHC, six cargo-binding tetratricopeptide repeats (TPRs), a C-terminal lipid-binding amphipathic helix, and an LFP motif that mediates KLC auto-inhibition (Figure 1A) (Anton, 2021; Cockburn et al., 2018; Morfini et al., 2016; Pernigo et al., 2018; Zhu et al., 2012). As a first step toward understanding developmental functions of KLC4, we investigated the expression of zebrafish *klc4* at different stages of development. Zebrafish *klc4* has two alternative splice isoforms, one long and one short, both of which are also present in other vertebrates including mice and humans. In zebrafish, the long *klc4* transcript encodes a full length protein of 620 amino acids while the short isoform is predicted to encode a 185 amino acid protein, ending just before the LFP motif (Figure 1 – figure supplement Figure1A). To determine whether both transcripts are expressed during development, we performed non-quantitative reverse transcriptase-PCR with transcript-specific primers on RNA extracted from embryos during early development (Figure 1B, Figure 1 - figure supplement 1A). We found that both isoforms are expressed throughout early development, with expression detectable at 2 hours post fertilization (hpf) and continuing through the initial period of neuronal axon outgrowth, pathfinding and branching, between 16 and 28 hpf (Figure 1B). We next used *in situ* hybridization to determine the spatial expression pattern of *klc4* during development, using a riboprobe that binds both transcripts. At 24 hpf, *klc4* is expressed in clusters of neurons in the telencephalon, epiphysis, diencephalon, ventral midbrain and hindbrain, and in the trigeminal and the posterior lateral line (pLL) ganglia (Figure1 C,D). In the spinal cord, *klc4* is strongly expressed in the Rohon-Beard sensory neurons, and at lower levels in other neuron populations (Figure 1E). At 48 hpf, *klc4* continues to be expressed broadly in the nervous system with high expression levels in the trigeminal ganglia, pLL ganglia, and RB neurons (Figure 1 F,G,H). The early expression of *klc4* in diverse neural populations in both the central and peripheral nervous system suggests it has functions in neural development.

Generation of *klc4* mutants

To assess the role of KLC4 during neural development, we used CRISPR/Cas9 to generate *klc4* mutants. We used a guide RNA targeting exon 3 of *klc4*, which encodes a part of the N-terminal heptad repeat region. One resulting allele, $klc4^{uw314}$, has a 25bp deletion in exon 3 from 404bp to 428bp in the heptad repeat region that leads to an early stop after 9 missense amino acids (Figure 1A, figure supplement 1B). Heterozygous $klc4^{uw314}$ mutants were outcrossed to wild type (AB strain) fish for three generations to remove any off-target mutations from the background. *In situ* hybridization analysis of homozygous $klc4^{uw314}$ mutant embryos showed virtually no *klc4* mRNA expression, suggesting that the mutant transcript undergoes nonsense-mediated decay (Figure 1I,J,K).

$klc4^{uw314}$ mutants show reduced branching of RB peripheral sensory axons

Because *klc4* is highly expressed in spinal RB sensory neurons, we first analyzed the effects of *klc4* mutation on their axon growth and morphology. We crossed the $klc4^{uw314}$ mutants with a transgenic line in which RB neurons are labeled with membrane-targeted GFP [*Tg(-3.1ngn1:gfp-caax)*] (Andersen et al., 2011) and used light sheet microscopy to image RB axon development across the whole embryo (Figure 2A,B). Inspection of mutant embryos revealed that RB peripheral axon branches appeared less dense and displayed less overall innervation of the sensory field compared to wild type (Figure 2A, B, Video 1, Video 2) To quantify these differences we labeled sensory neurons with anti-HNK1 antibody at 24 hpf (Figure 2C,D,E). We counted the number of branches that crossed an ROI at a standard distance

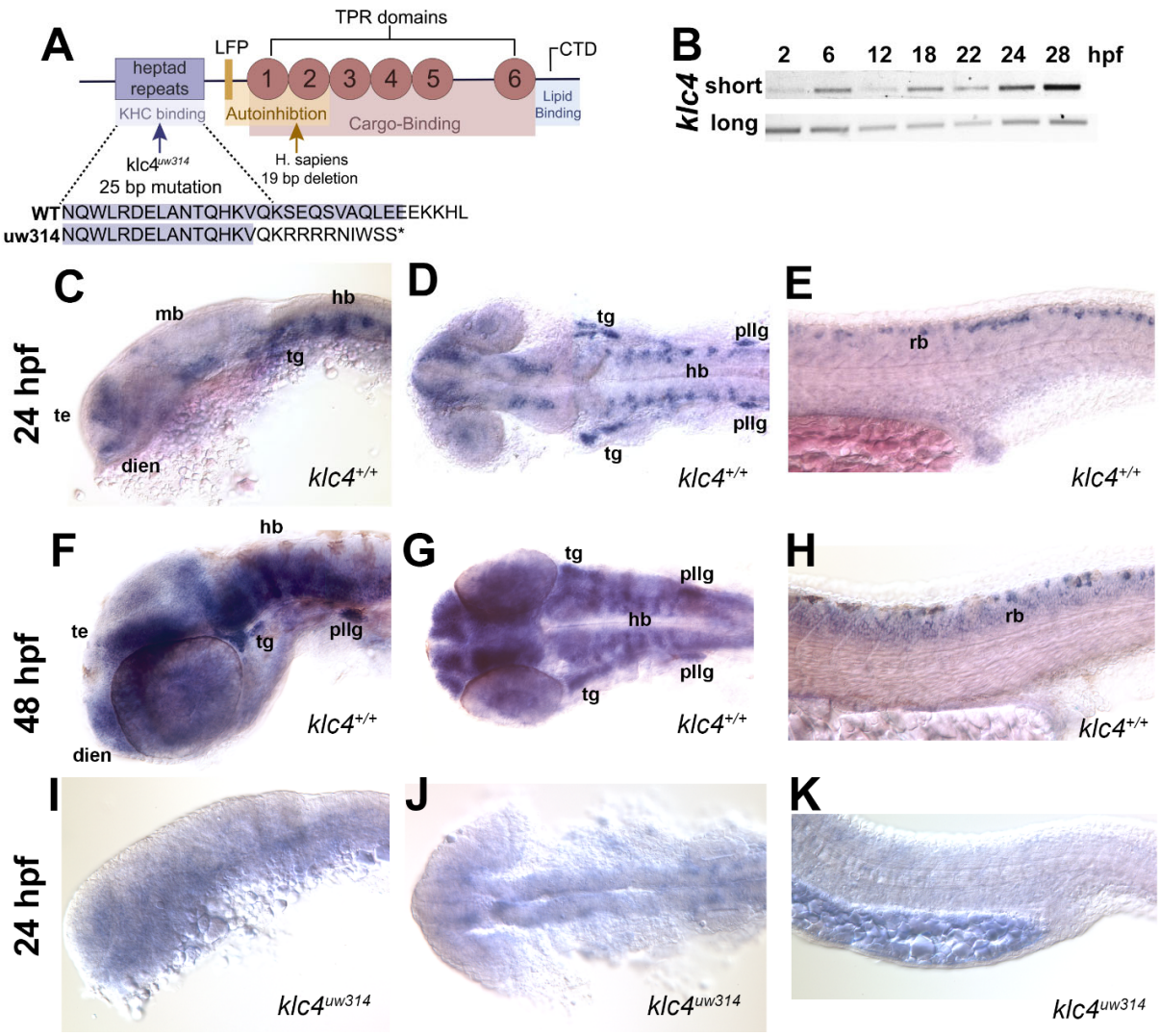

Figure 1. *klc4* mRNA is expressed in developing zebrafish embryos. **A)** Diagram of the highly conserved domains of KLC4. Arrows indicate where mutation occurs in humans and in our zebrafish mutant. **B)** Qualitative RT-PCR showing both long and short *klc4* isoforms are expressed throughout development. **C-D)** *In situ* hybridization for *klc4* mRNA shown in lateral view (**C**) or dorsal view (**D**) of the head in wild type 24 hpf embryos. **E)** Lateral view of trunk showing *klc4* expression in Rohon-Beard sensory neurons in a 24 hpf wild type embryo. **F-G)** *klc4* expression in the lateral view (**F**) or dorsal view (**G**) of the head of a 48 hpf wild type embryo. **H)** Lateral view of trunk showing *klc4* expression in the spinal cord of a 48 hpf wild type embryo. **I-K)** Lateral (**I,K**) and dorsal (**J**) views of *klc4 in situ* hybridization in 24 hpf *klc4*^{uw314} mutant embryo head (**I,J**) and trunk (**K**) showing little expression of *klc4*.

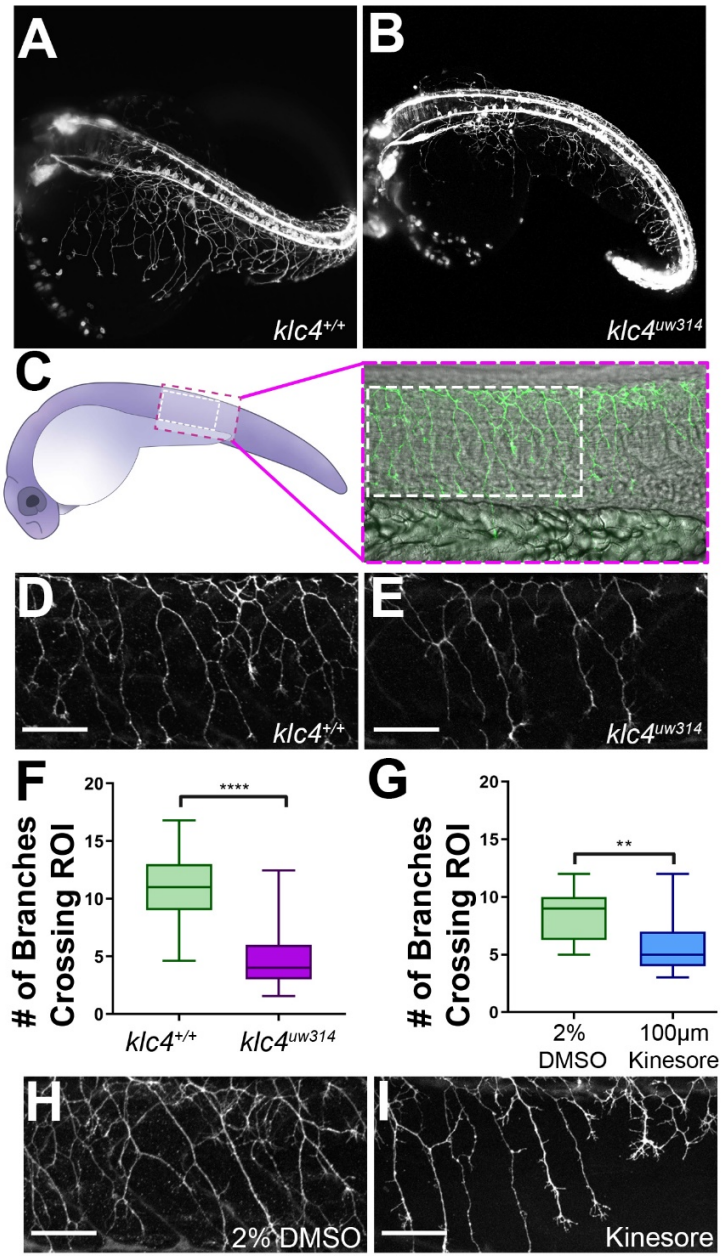

Figure 2. *klc4*^{uw314} mutants have reduced Rohon-Beard peripheral axon branching. **A-B)** Stills taken at approximately 24 hpf from long term light sheet movies of wild type (**A**) or *klc4*^{uw314} mutant (**B**) embryo development. **C)** Diagram of a 24 hpf embryo indicating the area over the yolk tube extension imaged for axon analysis, with the standard ROI used for analysis outlined by the white dashed rectangle. **D-E)** Representative examples of HNK-1 stained embryos showing peripheral axon branching in wild type (**D**) and *klc4*^{uw314} (**E**) embryos. **F-G)** Quantification of axon branching across three replicates in wild type (n = 30) and *klc4*^{uw314} mutant (n=30) embryos (**F**) and DMSO (n = 12) and kinesore (n = 19) treated embryos (**G**). **p=0.0025, ****p<0.0001, t-test. Error bars = 5-95th percentile. **H-I)** Representative examples of HNK-1 stained embryos showing peripheral axon branching in DMSO (**H**) and kinesore treated (**I**) embryos. All scale bars = 50 µm.

from the central axon fascicle (See Figure 2 -- supplemental figure 2). Consistent with our visual impression of reduced branching, wild type embryos had nearly three times more axons crossing the ROI than mutants (wild type average = 11.27 axons, *klc4*^{uw314} average = 3.77, Figure 2F).

As an alternative approach to understand the role of KLCs in axon branching, and to develop a more time-resolved means to disrupt KLC function, we took a pharmacological approach. Specifically, embryos were treated with Kinesore, a small molecule that has been shown to interfere with the interaction between the KLC TPR repeat domain and cargo adaptor proteins (Randall et al., 2017). We found that treatment of wild type embryos with 100 µM Kinesore during early stages of peripheral axon arborization, from 17 hpf to 24 hpf, caused a reduction in axon branch number at 24 hpf of a similar magnitude to that seen in *klc4*^{uw314} mutants (Figure 2G,H,I). These results give further evidence that properly regulated KLC-cargo interactions during axon outgrowth are important for successful axon branching.

KLC4 is required for stabilization of axon branches

To investigate which specific dynamic processes during branching are affected by *klc4* loss of function, we used live confocal imaging. Zebrafish RB axons branch by two mechanisms: growth cone bifurcation (GCB) and interstitial back branching (IB) (Gibson and Ma, 2011). To determine if GCB, IB or both were defective in mutants, we used the *Tg(-3.1ngn1:gfp-caax)* transgenic line (Andersen et al., 2011). Z-stacks of RB peripheral axon arbors were collected every 1-1.5 minutes for 2-4 hours beginning from approximately 18 hpf. The number of branch initiation and retraction events during a two-hour time window were counted and categorized as either a GCB (Figure 3A, white arrows) or IB event (Figure 3A, magenta arrows). Surprisingly, we found no difference in the rate of branch initiation between *klc4*^{uw314} mutant and wild type embryos (Figure 3C). In both conditions, new branches were initiated via GCB more frequently than IB, but there was no difference in the proportion of GCB versus IB branching events between wild type and *klc4*^{uw314} mutants.

Nevertheless, the live imaging immediately suggested an explanation for the branch number deficit: failure of branches to persist. That is, following formation, while most of the branches in wild type animals were relatively stable and continued growing (Video 3), those in the mutants often retracted after formation (Figure 3B, Video 4). Quantification showed that in *klc4*^{uw314} mutants, 57.7% of GCB branches and 61.9% of IB branches retracted after initiating, compared to 14.2% of GCB and 11.8% of IB branches in wild type (Figure 3D). This phenotype cannot be explained as a general axon growth defect, as *klc4*^{uw314} mutant axons grew at a faster rate than wild type axons (Figure 3E). Thus, these data suggest that KLC4 is required specifically for stabilization of axon branches.

Sensory axon arborization pattern is altered in *klc4*^{uw314} mutants

Peripheral sensory axons develop a distinctive arborization pattern to successfully innervate the sensory field. During this process, axons mutually repel each other upon contact (Liu and Halloran, 2005; Sagasti et al., 2005). Precise regulation of contact repulsion as well as branching are critical for effective tiling of the entire skin. To determine whether mutants have altered arborization and to quantify branching pattern in an unbiased manner, we developed an image analysis pipeline to measure axon directional orientation and overall axon abundance (Figure 4). We used OrientationJ (Rezakhaniha et al., 2011) to measure the fluorescence signal of aligned pixels at each orientation (Figure 4A,B) and created an axon directionality “profile” that represents the average signal at each 1.0 degree angle interval across multiple embryos (Figure 4C). In wild type embryos, most axons are

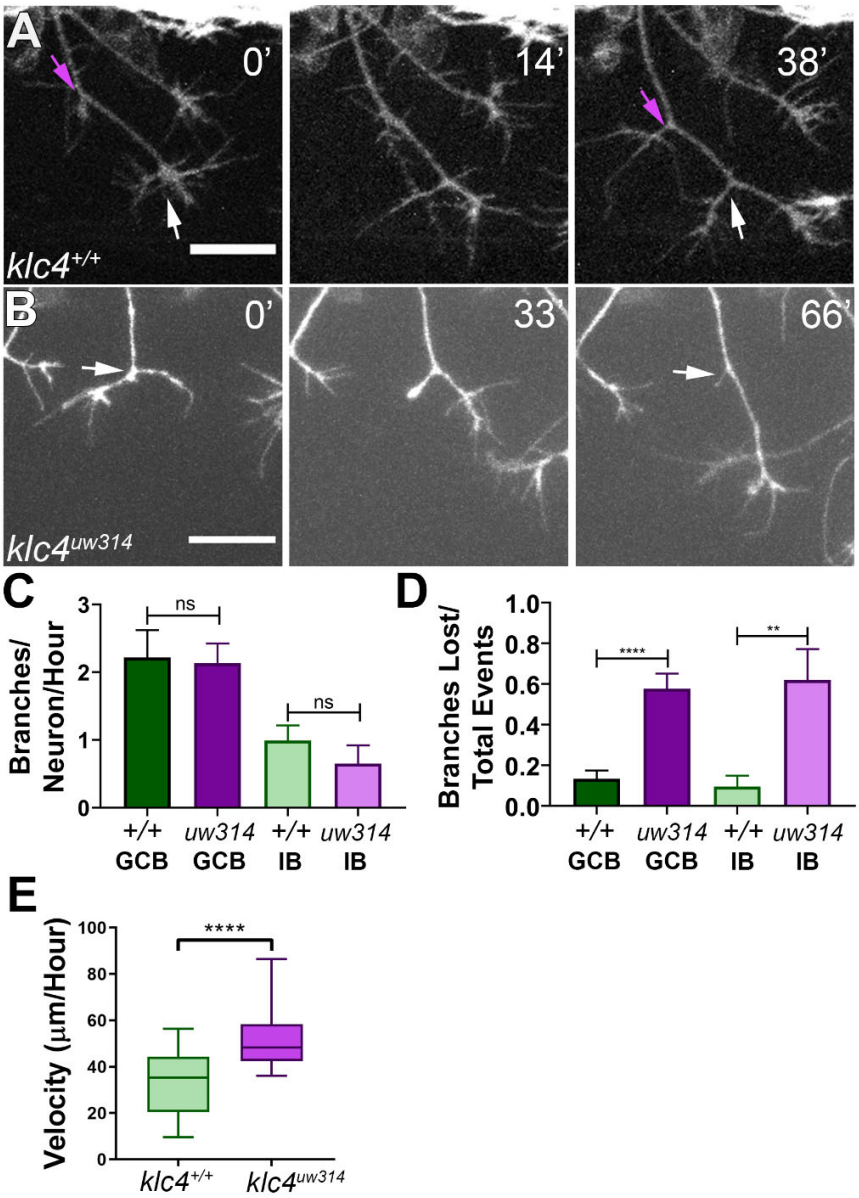

Figure 3. Branches initiate but do not stabilize in *klc4*^{uw314} mutants. **A)** A wild type axon forms stable branches by growth cone bifurcation (GCB, white arrows) and interstitial branching (IB, magenta arrows) over the course of 38' minutes. **B)** A *klc4*^{uw314} mutant axon initiates a branch via GCB (0 minutes, white arrow), but the branch begins to retract and is nearly fully gone after 66' minutes (panel 3, white arrow). 20 µm scale bar. **C)** Quantification of axon branch initiations per neuron per hour in wild type and mutant embryos (wild type GCB mean = 2.22 branches/neuron/hr, N = 11 neurons from 4 embryos. *klc4*^{uw314} GCB = 2.13 branches/neuron/hr, N = 14 neurons from 4 embryos. wild type IB = 0.99 branches/neuron/hr, N = 10 neurons from 4 embryos. *klc4*^{uw314} IB = 0.65 branches/neuron/hr, N = 8 neurons from 4 embryos). Error bars = SEM. There was no significant difference in branch initiation between wild type and mutant axons. GCB p = 0.73, IB p = 0.15, t-test with Mann–Whitney correction. **D)** Quantification of branches that retracted after initiation in wild type and *klc4*^{uw314} embryos. Data is displayed as a branch loss ratio (branches retracted/total branching events). Branches created by either GCB or IB were both more likely to retract in *klc4*^{uw314} embryos (wild type GCB mean = 0.13, N = 11 neurons from 4 embryos; *klc4*^{uw314} GCB = 0.58, N = 14 neurons from 4 embryos; wild type IB = 0.10, N = 10 neurons from 4 embryos; *klc4*^{uw314} IB = 0.62, N = 8 neurons from 4 embryos). **p=0.0055, ****p<0.0001, t-test with Mann–Whitney correction. Error bars = SEM. **E)** Quantification of axon growth velocity. Axons in *klc4*^{uw314} mutants grow faster than in wild type. Wild type N = 19 axons from 3 embryos. *klc4*^{uw314} N = 22 axons from 4 embryos. ****p<0.0001, t-test. Error bars = 5-95th percentile.

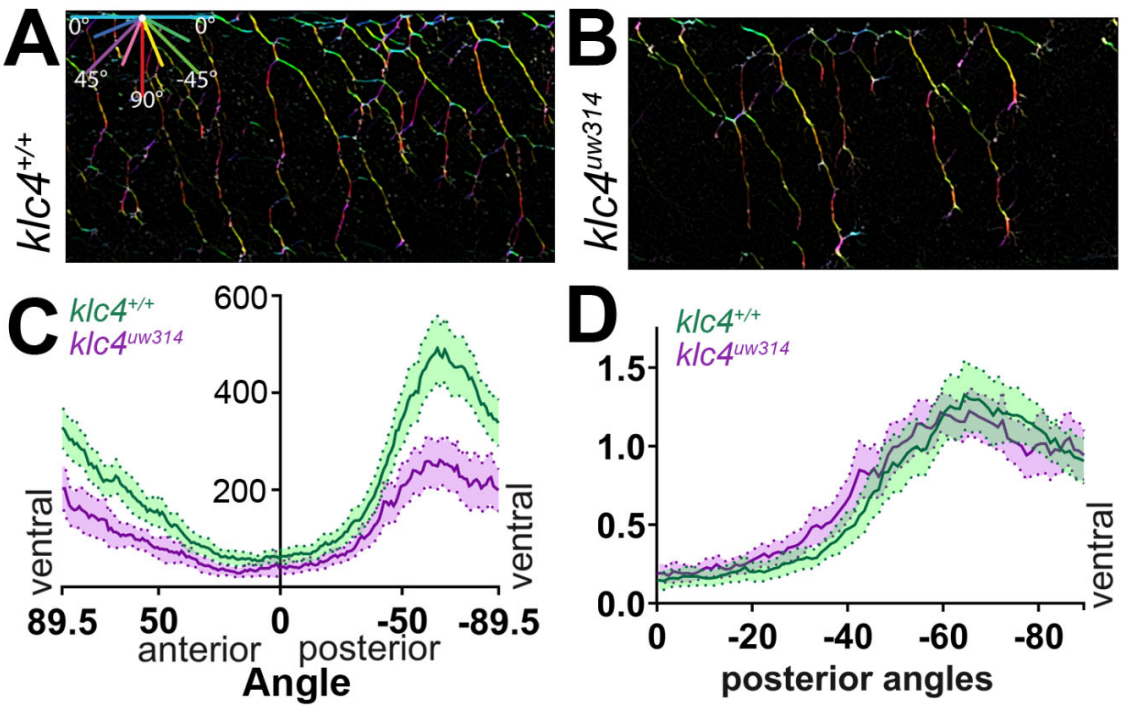

Figure 4. Axon orientation profiling reveals increased posterior directionality of peripheral axons in *klc4*^{uw314} mutants. **A-B)** A representative region of axon analysis for a 24 hpf wild type (**A**) and *klc4*^{uw314} (**B**) embryo. The axons are color coded for directionality according to the legend in the upper left corner of (**A**). **C)** Plot of axon directionality in 24 hpf wild type (green) and *klc4*^{uw314} mutants (magenta). **D)** Axon directionality data was normalized to total signal and posterior angles are displayed to compare directional bias. For **C-D**, error bars = 95% CI. Wild type N = 40 embryos, *klc4*^{uw314} N = 23 embryos.

oriented in ventral-posterior and ventral-anterior directions, with a higher proportion of axon signal in posteriorly directed angles, peaking between -50° and -80° (Figure 4 A,C, supplemental figure 4A). Little signal was detected in the horizontal (0 degrees) orientation. In contrast, *klc4*^{uw314} mutants had reduced overall axon signal compared to their wild type cousins (Figure 4B, C, supplemental figure 4B), consistent with the reduced branch density. Mutants showed an overall directional profile similar to wild type (Figure 4B,C). However, because differences in axon orientation between wild type and mutants may be masked by the overall difference in signal, we normalized the data and displayed it as a percentage of total signal at each angle. We found a small increase in axons oriented in the posterior direction in *klc4*^{uw314} mutants, specifically those oriented between -20° and -45° (Figure 4D). There was no difference in the proportion of anterior-directed axons between wild type and *klc4*^{uw314} mutants (Figure 4 – supplemental figure 4C).

To investigate what changes in axon behavior could generate the posterior orientation bias in mutants, we turned to live imaging. We first analyzed the growth direction of actively extending axons and branches by measuring the orientation angle of the distal-most axon shaft at each time point over 2-4 hour movies (Figure 5A) and displaying the distribution of growth angles as rose plots. We found *klc4*^{uw314} mutant axons had a preference for posterior growth paths, while wild type axons had no anterior-posterior bias (Figure 5B, C). We then measured the angles between newly bifurcating sister branches. Prior to branching, the main axon commonly grows in a posterior direction in both wild type and mutant embryos (Figure 5D). As axons branch in wild type embryos, the sister branches grow away from each other (Figure 5D',E, Video 5), resulting in an average branch angle of 96.5 degrees fifteen minutes after branch formation, and 91.7 degrees 75 minutes after branch formation (Figure 5E, G). This behavior drives the even anterior-posterior growth distribution seen in wild type embryos (Fig 4 C). In *klc4*^{uw314} mutants, the newly formed branches did not separate as much, resulting in a shallower average angle of 79.7 degrees between sister branches 15 minutes after branch formation, and narrowing to 60.2 degrees after 75 minutes (Figure 5 F,G, Video 6). In fact, branches in *klc4*^{uw314} mutants frequently failed to repel at all, instead appearing to collapse onto one another (see Figure 6B). These results suggest that KLC4 is involved in mediating mutual repulsion between sister axon branches. Moreover, the posterior growth bias detected by automated orientation analysis in *klc4*^{uw314} mutant embryos is very likely the result of branch repulsion failure. Since the main axons tend toward posterior growth, reduced branch repulsion or collapse of anteriorly directed branches onto the main axon shaft leads to an overall shift toward posterior directionality. Thus, our automated, population-scale method of axon orientation profiling led to the discovery of a branch repulsion defect, demonstrating the utility of the profiling method for revealing alterations in axon arbor pattern.

Peripheral axons in *klc4*^{uw314} mutants exhibit abnormal fasciculation behavior

Our live imaging also revealed a broader defect in contact repulsion: normally, in wild type embryos when a peripheral axon growth cone contacts another axon (either a branch of the same neuron or of another neuron) it retracts or changes direction to grow away from the other axon, thus minimizing contact between axons (Liu and Halloran, 2005; Sagasti et al., 2005) (Figure 6A). However, in *klc4*^{uw314} mutants, axons often fasciculate after such contacts and grow together for substantial distances (Figure 6B,C, Video 7). In some cases, axons were fasciculated so tightly that they only became distinguishable as two axons when pulled apart by the force of a developing branch (Figure 6B, arrows, Video 8). In wild type embryos, all observed fasciculations (n=3) resolved by retraction or defasciculation, but only 46.5% of fasciculations (n=19) in *klc4*^{uw314} mutants were resolved in this manner. Fasciculation behavior was quantified by measuring the frequency and length of

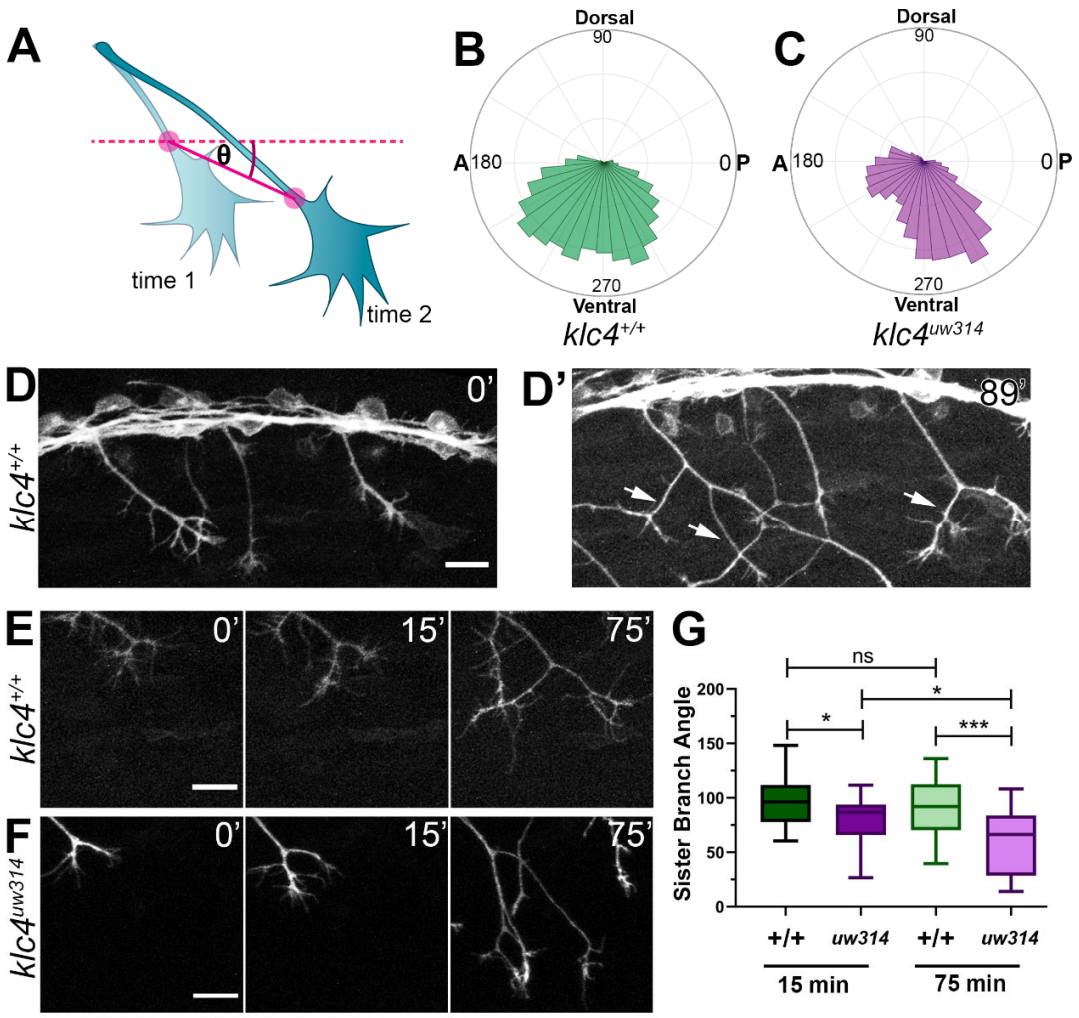

Figure 5. Live imaging shows that *klc4*^{uw314} mutants have a bias toward posterior growth direction and defective sister branch separation. **A)** Illustration of how axon growth direction was measured. The angle between an axon's position in each frame and the frame preceding it was measured. **B-C)** These angles were plotted as rose plots to show growth direction distributions. Wild type axons grow evenly between anterior and posterior directions, while *klc4*^{uw314} mutant axons show a preference for posterior directed growth. Wild type N = 19 axons from 3 embryos. *klc4*^{uw314} N = 22 axons from 4 embryos. **D)** Stills from a live capture of wild type axon outgrowth, showing that the main axon often grows posteriorly, but anterior directed branches form over time (**D',** white arrows). **E)** As a branch forms in a wild type peripheral axon, the angle between sister branches remains consistent as axons grow apart. **F)** In *klc4*^{uw314} mutants, sister branches do not grow apart and the sister branch angle narrows over time compared to wild type. All scale bars = 20 µm. **G)** Quantification of the angle between newly formed sister branches at 15 and 75 minutes after branch creation. Wild type 15' N = 37 branches, *klc4*^{uw314} 15' N = 36 branches, Wild type 75' N = 25 branches, *klc4*^{uw314} 75' N = 18 branches. 4 embryos per genotype. *p=0.021, ***p=0.0003, One-way ANOVA. Error bars = 5-95th percentile.

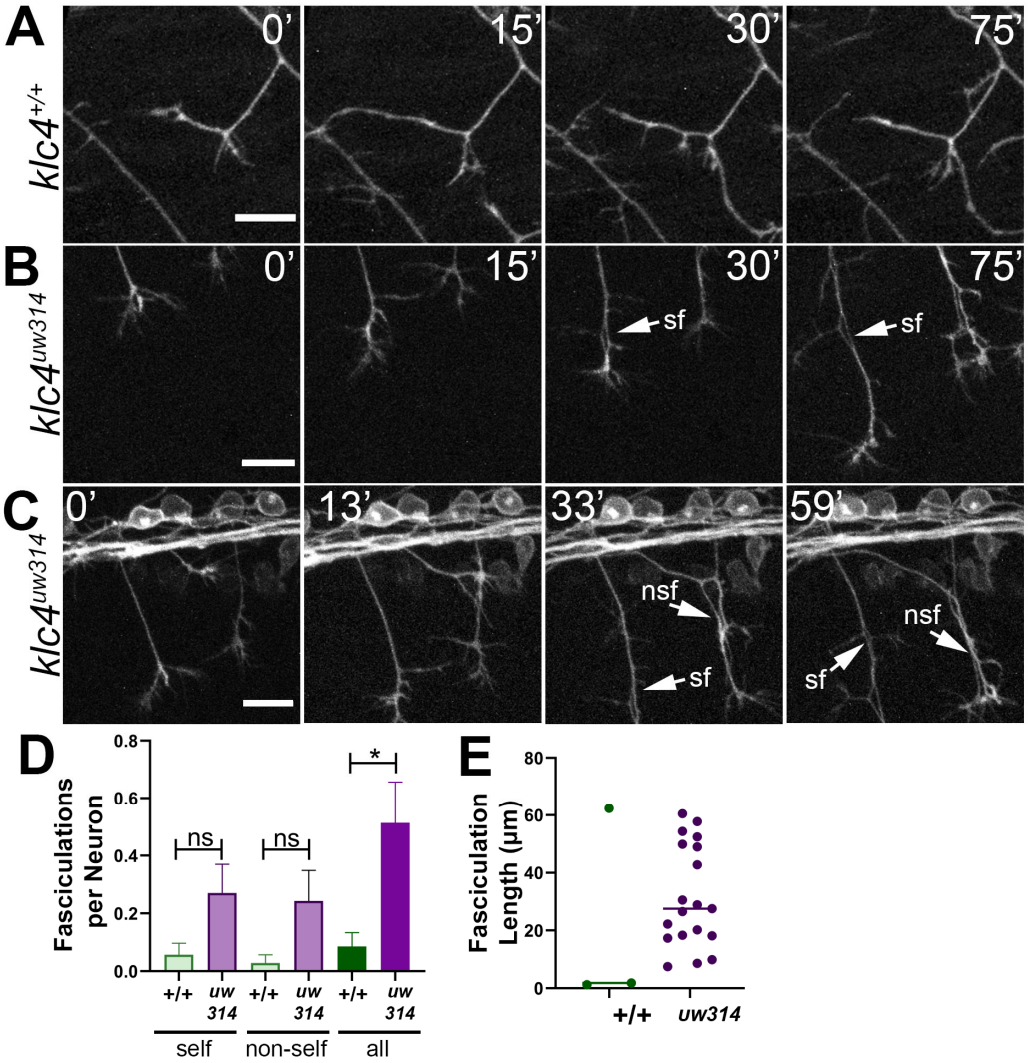

Figure 6. Loss of KLC4 results in aberrant axon fasciculation. **A)** In wild type embryos, the most common response to self or non-self contact between axons is retraction. Two neighboring axons in a wild type embryo make contact (time 0') and within 30 minutes, one of the axons has retracted. **B-C)** When axons make contact in *klc4*^{uw314} embryos, they often fasciculate instead of retracting. This happens with both self-contacts (**B-C,** sf) and non-self-contacts (**C**, nsf). All scale bars = 20 µm. **D)** Fasciculations per neuron, separated by self or non-self, as well as all fasciculations combined. Wild type N = 35 neurons in 4 embryos. *klc4*^{uw314} N = 37 neurons in 5 embryos. Error bars = SEM. **E)** Fasciculation length was measured from the last frame of each 2 hour imaging period. Wild type N = 3 fasciculations, *klc4*^{uw314} N = 19 fasciculations. Mean with 95% CI displayed over individual data points. Since fasciculation events are rare in wild type embryos, we could not apply a statistical test to assess the significance for the difference in fasciculation length.

252 fasciculation events occurring during our live imaging period. We found that fasciculation events were
253 rare in wild type embryos but occurred relatively frequently in mutants (Figure 6D). Fasciculations
254 ranged from 7.5-60.5 µm in length in *klc4*^{uw314} mutants (Figure 6E). Together, these results show that
255 KLC4 is important for the contact repulsion needed to shape sensory arbors. The mutual repulsion
256 normally exhibited by peripheral axons is in contrast to the fasciculation behavior of the central axons
257 from the same neuron. The failure of *klc4*^{uw314} mutant peripheral axons to show repulsion suggests that
258 KLC4 may be involved in the localization of factors controlling central versus peripheral axon
259 behavior.
260
261 **RB neurons have aberrant apical axons in *klc4*^{uw314} mutants**
262 RB neurons in *klc4*^{uw314} mutants also showed abnormal morphology suggestive of altered cell polarity.
263 We found that some RB neurons in *Tg(-3.1ngn1:gfp-caax)*;*klc4*^{uw314} mutant embryos and Kinesore
264 treated embryos projected a process from the apical cell body that crossed the midline within the
265 dorsal spinal cord (Figure 7A,B, Video 9, 10). Small apical protrusions sometimes form on RB neurons,
266 especially in the anterior portion of the spinal cord, though they can be found nearly anywhere along
267 the spinal cord. These processes are typically short, dynamic, and are most common early in
268 development (18-24 hpf) (Video 11). In wild type embryos, they rarely cross the midline of the spinal
269 cord. We counted the number of midline crossing apical processes from images of anti-HNK-1-labeled
270 embryos captured in the spinal cord overlying the yolk extension, and found that 4% of neurons
271 (n=1509 neurons in 51 embryos) in *klc4*^{uw314} mutants had midline crossing processes compared to 1%
272 in wild type embryos (n=608 neurons in 21 embryos) (Figure 7C). Similar results were obtained
273 following treatment with Kinesore from 18-24 hpf, with 7% of Kinesore-treated neurons (n=433
274 neurons in 17 embryos) extending an apical protrusion that crossed the midline, compared to 2% of
275 neurons in vehicle treated control (n=436 neurons in 15 embryos) (Figure 7C). To further assess
276 neuronal morphology and the pathways of the aberrant projections, we sparsely labeled individual RB
277 neurons by injecting DNA encoding TagRFP-caax driven by the -3.1ngn1 promoter at the 1-cell stage.
278 This mosaic cell labeling showed that the apical processes grew to and fasciculated with the
279 contralateral central axon fascicle in both *klc4*^{uw314} mutant and kinesore treated embryos (Figure 7D,F),
280 suggesting they may respond to cues directing central axon behavior despite emerging from an
281 ectopic apical location. These results suggest that KLCs have a role in determining the location of
282 axon emergence from the cell body.
283
284 **Microtubule dynamics are altered in *klc4*^{uw314} mutants**
285 Because local changes in MT dynamics are associated with axon branch formation, and MT invasion of
286 nascent axon branches is required for branches to be stabilized and maintained (Armijo-Weingart and
287 Gallo, 2017; Dent and Kalil, 2001; Gallo, 2011; Yu et al., 1994; Yu et al., 2008), we assessed whether the
288 MT cytoskeleton is affected in *klc4*^{uw314} mutants. To visualize MT dynamics *in vivo,* we used the MT plus-
289 tip binding protein EB3 fused to GFP (Stepanova et al., 2003). EB3-GFP binds to the plus ends of
290 actively polymerizing MTs, which appear as moving GFP puncta or "comets". We expressed EB3-GFP in
291 individual RB neurons by injecting *ngn1:EB3-GFP* DNA into embryos at the 1-cell stage. We used a high-
292 speed swept field confocal microscope that allows imaging of rapid MT polymerization events in 3D.
293 We captured z-stacks of RB axon arbors at 2-5 second intervals for periods ranging from 7-10 minutes
294 and used kymography to quantify microtubule dynamics (Figure 8A, Video 12). In axons, the majority
295 of comets move in the anterograde direction, reflecting the plus-end-distal organization of MTs. We
296 found no change in the percentage of retrograde comets between wild type and *klc4*^{uw314} mutants,
297 suggesting KLC4 is not necessary for organization of MT polarity (Figure 8 B,C). However, we found a

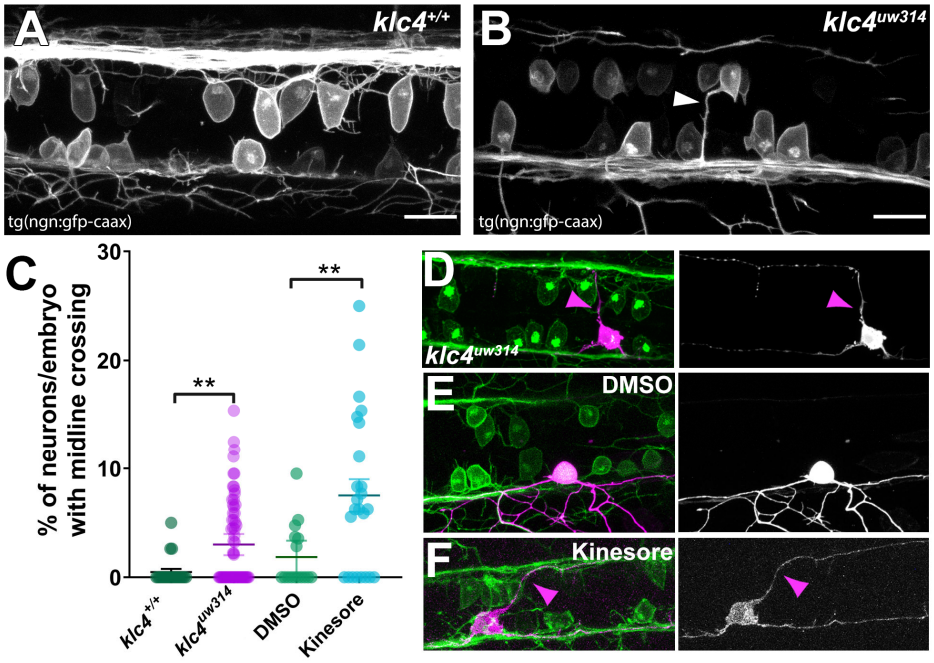

Figure 7. Midline crossing of apical protrusions occurs more frequently when KLC function is disrupted. **A-B)** Confocal projections (dorsal views) of partial z-stacks containing only the optical sections in the plane of the RB cell bodies within the spinal cord in a wild type Tg*(-3.1ngn1:gfp-caax)* embryo **(A)**, or a *klc4*^{uw314} Tg*(-3.1ngn1:gfp-caax)* embryo **(B),** with an apical protrusion from a neuron crossing the midline and reaching the contralateral side (white arrowhead). Scale bars = 20 μm. **C)** The percentage of neurons per embryo that had an apical protrusion crossing the midline of the spinal cord was quantified. **p<0.0052, t-test with Mann–Whitney correction. Mean with 95% CI displayed over individual data points. Wild type N = 608 neurons from 21 embryos, *klc4*^{uw314} N = 1496 neurons from 47 embryos, 2% DMSO N = 429 neurons from 15 embryos, Kinesore N = 595 neurons from 21 embryos. **D-F)** Mosaic labeling of individual neurons by injection with -3.1ngn1:gfp-caax DNA shows that apical protrusions (magenta arrowheads) can fasciculate onto the contralateral central axon.

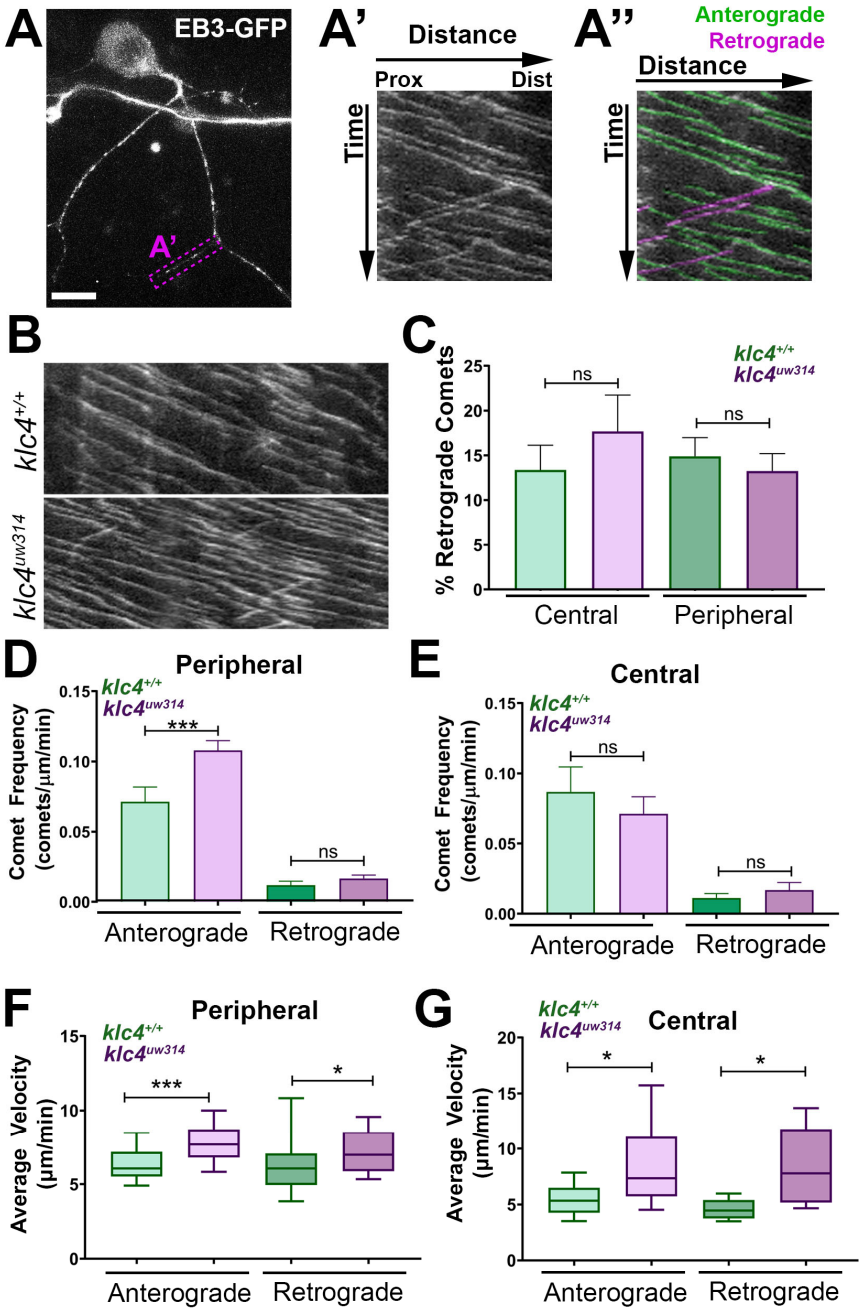

Figure 8. Microtubule dynamics are increased in *klc4*^{uw314} mutants. **A-A")** RB neuron expressing EB3-GFP. Magenta box in (**A**) indicates axon segment selected for kymograph in (**A'**). **A")** EB3 comets identified as anterogradely (green) or retrogradely (magenta) directed based on their angle. **B)** Representative kymographs from peripheral axon segments of wildtype (top) or *klc4*^{uw314} (bottom). **C)** Quantification of the percentage of retrograde comets out of all comets for both peripheral and central axons. NS by t-test with Mann–Whitney correction. **D)** Peripheral axon comet frequency. p***=0.0003, t-test with Mann–Whitney correction. **E)** Central axon comet frequency. NS by t-test with Mann–Whitney correction. **F)** Peripheral axon comet velocity. p***=0.0004, *p=0.042, t-test with Mann–Whitney correction. **G)** Central axon comet velocity. p*<0.05, t-test with Mann–Whitney correction. For all data, error bars = SEM. Wild type central N = 8 segments, *klc4*^{uw314} central N = 15 segments, Wild type peripheral N = 26 segments, *klc4*^{uw314} peripheral N = 48 segments. Wild type data from 10 neurons in 7 embryos. *Klc4*^{uw314} data from 13 neurons in 8 embryos.

298 significant increase in the frequency of anterograde comets in peripheral axons, but not central axons
299 of *klc4*^{uw314} mutant RB neurons (Figure 8B,D,E), suggesting increased MT dynamics in peripheral axons.
300 In addition, we found that the velocity of EB3-GFP comets, both anterograde and retrograde, was
301 increased in both peripheral and central axons in *klc4*^{uw314} mutants (Figure 8E,F), suggesting a role for
302 KLC4 in regulating the growth rate of MT plus ends. This disruption in MT dynamics may contribute to
303 the axon branch instability in *klc4*^{uw31} mutants.
304
305 **Adult *klc4*^{uw314} fish have morphological and behavioral defects**
306 The deficits found in development following loss of KLC function seemed likely to lead to deficits in
307 adult fish as well. Indeed, we found that *klc4*^{uw314} mutants are adult viable and fertile but are smaller in
308 size than their wild type siblings (Figure 9A). To measure body size in a controlled manner, we in-
309 crossed F4 homozygous *klc4*^{uw314} mutants from both AB and mixed AB/TL backgrounds and separately
310 in-crossed their wild type (AB) siblings. The F5 embryos were born on the same day, raised side-by-
311 side in an identical environment, and fed the same diet. We measured the body length of these fish at
312 7 weeks and at 9 weeks (Figure 9B). *klc4*^{uw314} mutants were on average 83.3% the size of their wild type
313 cousins at 7 weeks. This difference remained at 9 weeks, despite both the wild type and *klc4*^{uw314}
314 mutant fish increasing in size, with *klc4*^{uw314} mutant fish measured at 84.6% the length of their wild
315 type cousins. Smaller body size has also been reported in *klc1* mutant mice (Rahman et al., 1999),
316 supporting the idea that KLCs are important for post-embryonic growth of the animal.
317
318 The formation of functional neural circuits ultimately depends on the precise orchestration of cell
319 biological processes during neural development. The human disease caused by *KLC4* mutation shows
320 developmental onset, manifesting at 3 years of age (Bayrakli et al., 2015). Multiple neural systems are
321 affected in human patients, who have defects in vision, hearing, movement and cognition. Thus, we
322 analyzed adult behavior to investigate KLC4's role in neural circuit function. To ask if the mutant's
323 small size reflected a defect in feeding behavior, we assayed feeding ability (Howe et al., 2018). Adult
324 zebrafish were isolated in individual 1L tanks, then 50 larval zebrafish were added to each tank. The
325 fish were allowed to feed on the larvae for one hour, then removed from the tank to allow counting of
326 the remaining larvae. Wild type fish were effective feeders, eating on average 90% of available
327 zebrafish larvae (Figure 9C). In comparison, *klc4*^{uw314} mutants ate on average only 60% of the larvae
328 available. We noted that the mutant fish that performed the worst in the feeding assay underwent
329 bouts of freezing behavior during the assay. Upon introduction of the larvae to the tank, the fish
330 ceased movement for extended periods.
331
332 Freezing behavior in zebrafish in response to a novel environment has been previously described and
333 interpreted as increased anxiety (Khan et al., 2017; Maximino et al., 2010; Wong et al., 2010; Ziv et al.,
334 2013). To test whether *klc4*^{uw314} mutant fish show anxiety-like behavior, we used a novel tank diving
335 test, which is similar in principle to the open field test used in rodents (Maximino et al., 2010; Wong et
336 al., 2010). In this test, fish are introduced to a novel tank and allowed to explore. Zebrafish typically
337 prefer to stay in the lower zone of the tank initially, and once they become acclimated they begin to
338 explore the upper regions of the tank (Figure 9D). We introduced adult animals (7 months old) to a
339 novel tank and filmed their behavior for 3 minutes. Analysis revealed that 90.9% of wild type fish
340 explored the upper zone of the tank during the 3 minute window, compared to only 18.8% of the
341 *klc4*^{uw314} mutant fish (Figure 9E). Of the animals that did explore the upper zone, both wild type and
342 *klc4*^{uw314} mutant animals took an average of 100 seconds before their first cross into the upper zone
343 (Figure 9F). Wild type animals spent an average of 14 seconds in the upper region of the tank,

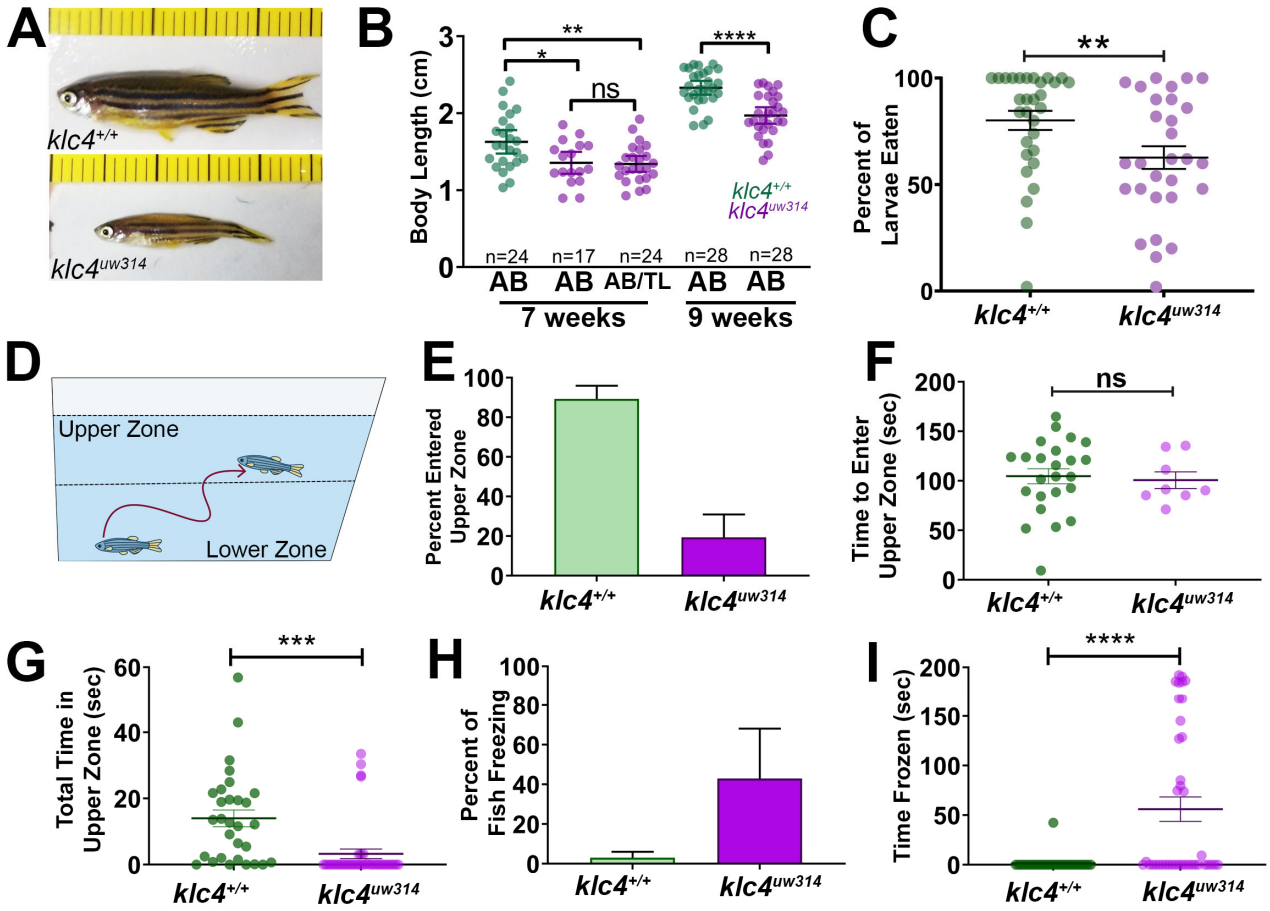

Figure 9. Adult *klc4*^{uw314} mutants have morphological and behavioral defects. **A)** Age-matched adult wild type and *klc4*^{uw314} mutant fish. Ruler tick marks represent 1mm. **B)** Body length measurements for age matched adult fish at 7 weeks and 9 weeks old. p****<0.0001, **p=0.0024, *p=0.013, t-test. N is given in figure as individual fish. **C)** Percentage of larvae consumed over an hour. **p=0.0090, t-test. Wild type N = 31, *klc4*^{uw314} N = 30. **D)** Schematic of the novel tank test design, with upper and lower zones demarcated by the center dotted line. **E)** Percentage of fish that entered the upper zone of the tank during a 3-minute exposure to a novel tank. Error bars = SEM. **F)** The time it took for individual fish to first cross into the upper zone during a 3-minute exposure to a novel tank. Points represent individual fish, error bars = SEM. Wild type N = 24, *klc4*^{uw314} N = 8. Fish that did not cross into the upper zone are not represented in this data. **G)** The total time fish spent in the upper zone of the novel tank during a 3-minute exposure. Points represent individual fish, error bars = SEM. Wild type N = 30, *klc4*^{uw314} N = 39. **H)** Percentage of fish to freeze during a 3-minute exposure to the novel tank. Error bars = SEM. **I)** The total time fish spent frozen during a 3-minute exposure to a novel tank. Points represent individual fish, error bars = SEM. Wild type N = 30, *klc4*^{uw314} N = 39. For **E** and **H**, wild type N = 3 experiments with 30 total fish, *klc4*^{uw314} N = 3 experiments with 39 total fish.

compared to just 3.26 seconds for *klc4*^{uw314} mutants (Figure 9G). Notably, freezing behavior, defined for this experiment as cessation of all movement except for gills for at least 3 seconds, was observed in an average of 43% of mutant fish, and only 3% of wild type fish (Figure 9H). 15.4% of *klc4*^{uw314} mutant fish, but no wild type animals, froze for the full 3 minute duration of the experiment (Figure 9I).

Studies in both zebrafish and rodents have shown that repeated exposure to the novel environment leads to habituation of the anxiety behavior. In zebrafish, habituation manifests as increased exploration of the upper zone and reduced freezing behavior. Fish that do not habituate to the novel environment or that worsen over multiple exposures are thought to demonstrate a depression-like phenotype (Ziv et al., 2013). Behaviors driven by increased anxiety are expected to lessen with repeat exposures. We tested the ability of *klc4*^{uw314} mutants to habituate to a novel environment after multiple exposures. In addition, because KLC4 and other kinesin-1 subunits have been implicated in neurodegenerative diseases, we sought to determine whether the anxiety-like behavior worsened with age. We challenged 1.25-1.5 year old *klc4*^{uw314} mutants and their wild type cousins by repeated exposure to a novel tank for 10 minutes, twice a week for 3 weeks in succession. The first exposure allowed us to test the effects of age. We found that increased age improved freezing response of *klc4*^{uw314} mutants, with only 29.2% (8 out of a total of 23) of individuals tested freezing for more than 3 seconds during first 3 minutes of exposure to the novel tank (Figure 10A). Aged wild-type animals worsened in performance, with 13.3% (3 out of 23) undergoing a bout of freezing behavior during first exposure. These numbers remained similar when the entire 10 minutes was analyzed (wt = 16.7%, mut = 29.2%, Figure 10B, supplemental figure 10A). Mutant fish spent a longer period of time frozen than wild type fish and underwent more total bouts of freezing per fish (Figure 10C, supplemental figure 10B). Upon subsequent exposures to the same tank, *klc4*^{uw314} mutant freezing behavior worsened (Figure 10B, supplemental figure 10A,B), with 50% of *klc4*^{uw314} mutants freezing by the sixth exposure, indicating that mutants fail to habituate freezing behavior. Mutants consistently froze for longer periods of time than wild type animals throughout all exposures (Figure 10B,C). Wild type animals performed approximately equally through subsequent exposures, undergoing less frequent freezing bouts and spending less time frozen than mutants (Figure 10B,C, supplemental figure 10A,B). Wild type fish also swam faster than *klc4*^{uw314} mutants, and showed similar swim velocities when their total swim velocity (including pauses) was compared to their mobile swim velocity (with pauses in swimming subtracted) (Figure 10D). *klc4*^{uw314} swim mobile swim velocity was faster than their total swim velocity, reflecting that they spent a greater amount of time immobile (Figure 10D).

Interestingly, both wild type and *klc4*^{uw314} mutants did show habituation as measured by the percentage of time spent in the upper zone of the tank (Figure 10E). During the first exposure, mutant animals only spent 8.7% of the ten minute experiment window in the upper zone and took on average 170.2 seconds before exploring the upper zone. Wild type animals explored the upper zone after an average of 80.0 seconds and spent 17.6% of the first exposure period in the upper zone (Figure 10E,F). At the time of the sixth exposure, however, both wild type and *klc4*^{uw314} mutants increased their time spent in the upper zone, and mutants entered the upper zone faster than in their first exposure (Figure 10E,F). Wild type animals took on average 79.7 seconds to explore the upper zone and spent an average of 25.4% of the experiment period in the upper zone. *Klc4*^{uw314} mutants performed similarly, spending 23.1% of the experiment period in the upper zone, but taking on average 129.0 seconds to explore the upper zone (Figure 10E). Thus, the failure of *klc4*^{uw314} mutants to habituate freezing is specific rather than reflecting a general deficit in habituation.

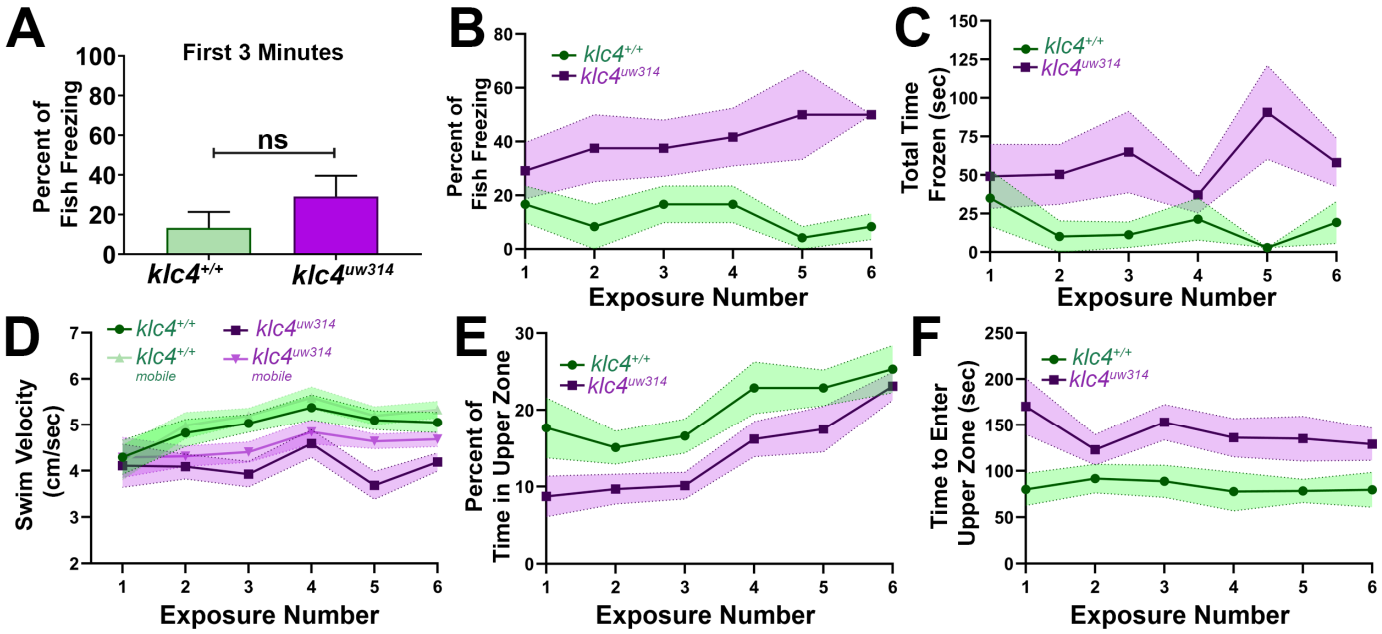

Figure 10. Adult *klc4*^{uw314} mutant anxiety-like behavior does not fully habituate after repeat exposure to a novel environment. **A)** Percentage of fish that froze during the first 3 minutes of a 10-minute initial exposure to a novel tank. **B)** Plot of the percentage of fish that froze during the course of six 10-minute exposures to the same novel tank. **C)** Plot of the average time spent frozen during the course of six 10-minute exposures to the same novel tank. **D)** Plot of the average total and mobile-only swim velocities of fish during each of six 10-minute exposures to the same novel tank. Mobile-only velocity excludes periods of time the fish spent at a velocity of 0 cm/sec (frozen). **E)** Plot of the percentage of time that fish spent in the upper zone of the tank during the course of six 10-minute exposures to the same novel tank. **E)** Plot of the average time it took for a fish to first enter the upper zone of the tank during the course of six 10-minute exposures to the same novel tank. For all data, N = 4 groups per genotype, 23 total fish per genotype. Error bars = SEM. For figures D-F, videos that could not be automatically tracked were omitted (for wild type, 6/138, for *klc4*^{uw314}, 4/138)

Discussion

The association of KLC4 with human disease demonstrates its critical importance, yet its cellular and developmental functions are poorly understood. In this study, we used automated analysis of sensory axon arbors and live, *in vivo* imaging of axon behavior and intracellular MT dynamics to define new roles for KLC4 in shaping neuronal morphology. We found that KLC4 is required for sensory axon branching and for contact repulsion between peripheral axons, behaviors which are important for proper innervation and tiling of the sensory field. *klc4* mutant neurons do not have a general growth defect, in that their axons grew faster than wild type axons. In addition, *klc4* mutants are adult viable and showed no signs of early neurodegeneration. These results suggest that KLC4 has a specific function in patterning developing neurons rather than simply being required for general neuronal health. Behavioral analysis showed that *klc4* mutant adults exhibit increased anxiety-like behavior, indicating roles for KLC4 in adult circuit function and identifying KLC4 as a novel gene associated with anxiety behavior. This work sheds light on potential mechanisms of human HSPs and provides a new animal model uniquely suited to further investigation of the cell biological and circuit mechanisms underlying disease.

Precise regulation of axon branching is critical for neurons to develop diverse and complex architecture. We identified KLC4 as a novel regulator of axon branching and show that it is required for stabilization of nascent branches. Axon branching requires extensive cytoskeletal rearrangements (Gallo, 2011; Kalil and Dent, 2014; Winkle et al., 2016). Branches begin as actin-based filopodial protrusions, which must be invaded by MTs to mature into branches. MT severing by proteins such as katanin and spastin is required to facilitate invasion (Qiang et al., 2010; Yu et al., 1994; Yu et al., 2008) and branch points are hot spots of increased MT dynamics (Dent and Kalil, 2001). Local unbundling of MTs in the axon shaft occurs at sites of interstitial branch formation (Kalil and Dent, 2014; Ketschek et al., 2015). Our finding that MT dynamics are affected in *klc4* mutants supports the idea that KLC4 could promote branch stabilization in part by regulating MT invasion into branches or MT crosslinking. Kinesin-1 can bind MTs via the KHC C-terminal tail and crosslink or bundle MTs (Navone et al., 1992; Seeger and Rice, 2010). Binding of KLC to KHC releases the autoinhibition of KHC and can tip the balance between kinesin-1's cargo transport activities and the ability of the KHC tail region to bind MTs (Cai et al., 2007; Chiba et al., 2021; Wong and Rice, 2010). Our data are consistent with a model in which KLC4 promotes the increased MT dynamics or severing that allows MT branch invasion. It could potentially do this by transporting/localizing MT regulators or by facilitating MT unbundling. In this model, loss of KLC4 would lead to MTs that stably associate and grow in a bundle, which could manifest as increased velocity and/or frequency of EB3-GFP comets. This model is also supported by the similarities in phenotype between *klc4* mutants and kinesore treatment. Kinesore blocks binding between KLCs and cargo adaptors, and also drives KHC toward increased MT bundling function (Randall et al., 2017).

In addition to cytoskeletal remodeling, regulated organelle/cargo transport and membrane remodeling are important for axon branching (Winkle et al., 2016), although little is known about how individual regulators of trafficking contribute to branching patterns. KLC4 could promote branching by delivering necessary cargos to nascent branches. For example, successful axon branch formation requires mitochondria to be localized to branch points to support branch growth (Courchet et al., 2013; Spillane et al., 2013; Tao et al., 2014; Wong et al., 2017). In addition, we previously found that a properly functioning endosomal trafficking system is necessary for RB axon branching (Ponomareva

et al., 2016; Ponomareva et al., 2014). Moreover, we showed that the kinesin adaptor Clstn1 is required for branching of peripheral RB axons and that it functions in part by trafficking endosomal vesicles to branch points (Ponomareva et al., 2014). KLC4 potentially could influence transport or localization of endosomes or mitochondria, either directly or by transporting other organelles that support mitochondria, such as ER, which is a critical regulator of mitochondrial function (Csordas et al., 2018; Krols et al., 2016; Rowland and Voeltz, 2012). An important future research goal is to determine whether KLC4 localizes specific organelles to branch points.

To maximize coverage of an innervation field, the axonal or dendritic arbors of neuronal populations that share a similar function must repel one another on contact to "tile" the field (Grueber and Sagasti, 2010; Spead and Poulain, 2020). Our results show that KLC4 is an important player in contact repulsion between sensory axons, and to our knowledge KLC4 is the first motor protein shown to be involved in tiling. Several cell surface or secreted proteins that meditate dendritic tiling have been identified, including protocadherins (Kostadinov and Sanes, 2015; Lefebvre et al., 2012), DSCAM (Matthews et al., 2007; Soba et al., 2007), netrin (Smith et al., 2012), and slit/robo signaling (Gibson et al., 2014). Less is known about the mechanisms of axon tiling, although similar molecules appear to be involved. For example, in *Drosophila*, DSCAM mediates sister branch separation in mushroom body axons (Wang et al., 2002), and Dscam2 mediates repulsion between axons in the visual system (Millard et al., 2007). An atypical cadherin, Flamingo, is required for spacing of photoreceptor axon arbors (Senti et al., 2003), and functions together with the transmembrane protein Golden goal (Hakeda-Suzuki et al., 2011; Tomasi et al., 2008). More recent studies have shown that the protocadherin PcdhaC2 mediates repulsion between axons of serotonergic neurons in the mammalian brain (Chen et al., 2017; Katori et al., 2017). Thus, the field has seen multiple advances in knowledge of the membrane proteins that mediate repulsion. However, the mechanisms that regulate their localization to the correct cellular compartments are unknown. Our work can drive new exploration into such mechanisms. For example, it will be interesting to determine whether KLC4 mediates transport of contact repulsion molecules and their specific targeting to peripheral versus central sensory axons.

The formation of polarized neuronal structure is a critical component of proper neural circuit development. An important early step in neuronal polarity development is determination of the location of axon emergence from the cell body. The ectopic apical axons we see in *klc4* mutants suggest that KLC4 also has roles in the polarity of axon initiation location. RB neuron axons normally emerge from basal edge of cell body (Andersen et al., 2011), and their emergence correlates with centrosome movement to the basal region of the cell (Andersen and Halloran, 2012). We previously found that *laminin-1* mutants also have ectopic apical axons in RB neurons and these ectopic axons correlate with apically displaced centrosomes (Andersen and Halloran, 2012). Laminin has been shown to influence the location of axon emergence from the cell body in zebrafish RGCs (Randlett et al., 2011), and can direct the positioning of the centrosome in neurons *in vitro* and *in vivo* (Gupta et al., 2010; Randlett et al., 2011). KLC4 may play a role in coordinating the response to extracellular signals such as laminin that help define site of axon formation.

Overall, the developmental phenotypes seen in *klc4*^{uw314} mutants are striking in that they appear to reflect problems with specific patterning of neuronal structure rather than problems in bulk cargo transport. Neurons appear healthy in the mutants, show no signs of axon degeneration during development, and in fact axons grow faster in mutants than in wild type embryos. Moreover, the *klc4*^{uw314} mutants are adult viable. Interestingly, *klc1* knockout mice are also adult viable and show

482 specific defects in transport of cannabinoid receptors in developing axons (Saez et al., 2020). Thus our
483 findings may reflect a general theme, that the function of the KLC subunits of the kinesin-1 motor are
484 to provide specificity to the process of localizing cargos to particular cell regions. Our results also give
485 insight into mechanisms of the human disease caused by *KLC4* mutation, which may be caused by
486 defects in developmental patterning. It will be important to fully define the unique cellular functions
487 of individual KLCs in order to better understand mechanisms of disease.
488
489 Adult circuit function can be affected by both defects in circuit development and/or later defects in
490 the function of neurons within circuits. Our finding that *klc4*^{uw314} mutant adults show freezing and
491 reduced exploration in the novel tank assay implicates KLC4 in the circuits that regulate stress
492 response and that are affected in anxiety and depression disorders. The hypothalamic-pituitary-
493 adrenal (HPA) axis is an important system that mediates stress responses, and zebrafish mutants with
494 disruptions to the HPA also exhibit anxiety behavior in the novel tank test. Mutation of zebrafish
495 glucocorticoid receptor, a target of the stress hormone cortisol, results in increased freezing and
496 decreased exploratory behavior. Like *klc4*^{uw314} mutants, glucocorticoid receptor mutants fail to
497 habituate freezing behavior after repeated exposures to the novel tank (Ziv et al., 2013). However,
498 unlike *klc4*^{uw314} mutants, glucocorticoid receptor mutants do not habituate exploratory behavior over
499 multiple exposures. This suggests that freezing behavior and exploratory behavior are controlled by
500 different mechanisms. Interestingly, zebrafish with mutation in a chemokine gene expressed in
501 multiple brain regions, *sam2*, freeze during the novel tank test, but show normal tank exploration
502 (Choi et al., 2018), providing additional evidence that these two behaviors can be uncoupled. The
503 *sam2* mutants have disruptions in corticotropin releasing hormone neurotransmission, linking the
504 mutation to HPA disruption, but not excluding contribution from other circuits. Our *klc4*^{uw314} mutants
505 provide another tool to further investigate the circuit changes underlying anxiety disorders.
506
507 Whether developmental defects in RB neurons contribute to adult circuit function is unknown. RB
508 neurons are traditionally thought to be a transient cell population that undergoes programmed cell
509 death during larval stages. However recent evidence has shown that 40% of RBs are maintained for at
510 least the first 2 weeks of development, suggesting they may be retained (Williams and Ribera, 2020).
511 Moreover, RB neurons have been shown to play significant roles in regulating larval behaviors (Knafo
512 et al., 2017). Hypersensitivity to touch is a common trait of autism spectrum disorder (ASD), although
513 the relationship of somatosensory neurons to states like anxiety, depression, and hyperstimulation is
514 not well defined. Interestingly, deletion of the ASD risk genes Mecp2 and Gabrb3 in mouse primary
515 somatosensory neurons during development led to a reduction in exploratory behavior in the open
516 field test, while deletion of these genes only during adulthood caused no such impairment or anxiety
517 behavior (Orefice et al., 2016). In addition to sensory neurons, *klc4* is expressed in many cell types in
518 the developing nervous system and thus likely has important roles in development and function of
519 other neurons, which may include neurons that are directly involved in circuits mediating adult
520 behavior. A future research goal is to test the functions of KLC4 in neurons of stress response circuits,
521 such as the HPA axis.
522
523 **Methods**
524 **Animals**
525 Adult zebrafish (Danio rerio) were kept in a 14/10 h light/dark cycle. Embryos were maintained at
526 28.5°C and staged as hours postfertilization (hpf) as described previously (Kimmel et al., 1995). Wild
527 type AB strain or transgenic Tg(−3.1ngn1:GFP-CAAX) (Andersen et al., 2011) (AB/TL background)

528 embryos were used for all experiments. All animals in these studies were handled in accordance with
529 the National Institutes of Health Guide for the care and use of laboratory animals, and the University
530 of Wisconsin Institutional Animal Care and Use Committee (IACUC). These studies were approved by
531 the University of Wisconsin IACUC.
532
533 **CRISPR/Cas9 mutagenesis**
534 A guide RNA targeting zebrafish *klc4* (5'-GAGCGTGGCACAGCTGGAGGAGG-3') was designed by using
535 CRISPRScan (crisprscan.org) and synthesized as previously described (Shah et al., 2015). To generate
536 *klc4*^{uw314} mutants, embryos at the very early 1 cell stage were injected with 374.5 ng/µl of the guide
537 RNA targeted to zebrafish *klc4* complexed with 800 ng/µl of Cas9 protein with NLS (PNA Bio). Injection
538 volume was approximately 1nL. F0 adult fish were pair-mated to determine individuals carrying germ
539 line mutations. A subset of individuals with germ line mutations were outcrossed to wild type AB fish.
540 F1 fish were raised and genotyped by PCR and sequencing, using CRISP-ID
541 (http://crispid.gbiomed.kuleuven.be/) to assist in sequence unmixing. The *klc4*^{uw314} allele was found to
542 have a 25 bp deletion. Fish heterozygous for *klc4*^{uw314} were outcrossed to wild type AB fish until the F3
543 generation. F3 *klc4*^{uw314} heterozygotes were in-crossed to generate F4 *klc4*^{uw314} homozygotes. All
544 homozygous mutants in this study were F5-F6 generation mutants from homozygous parents, unless
545 otherwise specified. Adults and embryos described as "wild type cousins" of *klc4*^{uw314} mutants were
546 generated by crossing F4 *klc4*$^{+/+}$ siblings from the F3 *klc4*$^{uw314/+}$ in-cross.
547
548 **RT-PCR**
549 RNA was extracted from zebrafish embryos at specified ages with Trizol (Thermo-Fisher), followed by
550 chloroform extraction and isopropanol precipitation. cDNA was generated from embryo-derived RNA
551 using the Superscript III reverse transcriptase kit and a 50:50 mixture of oligo dT and random hexamer
552 primers (Invitrogen). We designed PCR primers to amplify specific *klc4* isoforms. A reverse primer
553 unique to the short isoform's 3' UTR was designed for the *klc4* short isoform, with the forward primer
554 in exon 2 (Fwd: 5'-GCGCAAATCAGTGGAGATGATAGAGC-3', Rev: 5'-GCATAGTGGCGCGGTAGGTA-3'). A set
555 of primers for exons exclusive to the long isoform of *klc4* (spanning exons 7 through 12) was designed
556 for the long isoform (Fwd: 5'- CAGAGAGAAGGTGCTGGG -3', Rev: 5'- GGTGGTGTTCACTGTTGG-3'). PCR
557 was then run to test for presence of the isoforms in cDNA from each embryonic age.
558
559 ***in situ* hybridization**
560 A digoxigenin-labeled riboprobe complementary to a region spanning exons 2-3 of the *klc4* mRNA,
561 which are contained in both long and short isoform mRNAs, was synthesized by in vitro transcription
562 using T7 RNA polymerase with a DIG RNA labeling kit (Roche). The template for transcription was
563 made using PCR on zebrafish cDNA with the following primers: Fwd: 5'-
564 GCGCAAATCAGTGGAGATGATAGAGC-3', Rev: 5'-TAATACGACTCACTATAGCTCCAGATGTTTCTTCTCCTCC-
565 3'. Whole-mount in situ hybridization was performed as previously described (Halloran et al., 1999).
566
567 **Immunohistochemistry**
568 Embryos were fixed overnight at room temperature in 4% paraformaldehyde in 0.1M PO_4 buffer, then
569 rinsed with PBS/0.1% Tween-20 (PBST) and blocked with incubation buffer (IB: 2mg/mL BSA, 1%
570 Sheep Serum, 1% DMSO, 0.5% Triton X-100 in PBS) for at least 1 hour. Embryos were incubated
571 overnight at 4°C with monoclonal anti-HNK1 antibody in IB (ZN-12, 1:250; Zebrafish International
572 Resource Center), rinsed in PBST, then incubated with anti-mouse AlexaFluor 488 secondary antibody
573 (1:1000; Invitrogen) for at least 2 hours at room temperature or overnight at 4°C.

574
575 **Microinjection and Mosaic Expression**
576 DNA expression constructs were made using the Multisite Gateway Cloning System (Invitrogen) into
577 Tol2 vectors (Kwan et al., 2007). Zebrafish embryos at the 1-cell stage were injected with ~10 pg -
578 *3.1ngn1:EB3-GFP* DNA (Lee et al., 2017) to visualize microtubule dynamics. For experiments to image
579 individual neuron morphology, embryos were injected with ~12pg *3.1ngn1:mCherry-CAAX* DNA
580 (Andersen et al., 2011).
581
582 **Kinesore treatment**
583 Kinesore was acquired from the Hit-2-Lead library (Chembridge, compound #6233307) and suspended
584 in DMSO for a stock concentration of 100 mM. Embryos treated with Kinesore were dechorionated at
585 17 hpf and placed in E3 containing 150 µM Kinesore and 2% DMSO. Controls were treated with 2%
586 DMSO in E3 for the same time period.
587
588 **Live Imaging**
589 Light sheet imaging was performed on a custom multi-view light sheet microscope as described in
590 Daetwyler et al, 2019. The detection objective was either an Olympus UMPLFLN 10x W (NA 0.3) or a
591 Nikon 25x W (NA 1.1) with a 400mm tube lens for 50x total magnification. Briefly, the Tg(*3.1ngn1:GFP-*
592 *CAAX*) wild type or mutant embryos were mounted in an FEP tube (0.8 mm inner diameter, 1.2 outer
593 diameter, Bola) suspended in 0.02% tricaine in E3 with an agarose plug to prevent leakage. For live
594 confocal imaging, embryos were anesthetized in 0.02% tricaine and mounted in 1% low melting
595 agarose in 10 mM HEPES E3 medium as described previously (Andersen et al., 2010). Axon outgrowth
596 was imaged in Tg(*3.1ngn1:GFP-CAAX*) embryos with either an Olympus FV1000 laser-scanning confocal
597 microscope using a UPlanSApo 20x Oil objective (NA 0.85) or an Opterra Swept-Field confocal (Bruker
598 Nano Surfaces FM) with a Nikon S Fluor 40x Oil immersion objective (NA 1.30). Imaging was started
599 between 18 and 19 hpf, when peripheral RB axons are extending out of the spinal cord. Optical
600 sections (1-1.25 µm) covering a 30–36 µm Z depth were captured every 60-90 s for 2-4 hours.
601 High speed imaging of EB3-GFP comets was performed with the Opterra Swept-Field confocal
602 microscope equipped with a Nikon Plan Apo VC 100x oil immersion objective (NA 1.40). Embryos were
603 imaged at stages between 18 and 26 hpf, during peripheral axon outgrowth. Z-stacks of 5–30 1-µm
604 optical sections were captured at 2–5 s time intervals, for total durations between 7 and 10 min.
605
606 **Axon Outgrowth Analysis**
607 To measure the speed of axon outgrowth, the area immediately behind the growth cone was
608 measured using the Manual Tracking plugin in FIJI (Fabrice Cordelières). The generated data was
609 loaded into the Chemotaxis and Migration Tool (Ibidi, https://ibidi.com/chemotaxis-analysis/171-
610 chemotaxis-and-migration-tool.html) to generate velocity measurements and rose plot histograms.
611 Rose plots were re-plotted in MATLAB (MathWorks) using secplot (Matthew Foster,
612 https://www.mathworks.com/matlabcentral/fileexchange/14174-secplot).
613
614 **Branch Analysis and Kymography**
615 Custom macros for FIJI (Schindelin et al., 2012) were written to automate branch analysis. Briefly,
616 stacks were processed to be maximum intensity projections and oriented with anterior to the left. A
617 rectangular ROI was selected over the posterior region of the yolk tube extension such that the top of
618 the selection was aligned with the bottom of the central RB axons. A tubeness filter was applied to
619 reduce non-axonal background. A histogram of axon directionality was generated for the ROI using

OrientationJ (Rezakhaniha et al., 2011). To measure axon branch density, a second 3 µm ROI was generated with its upper boundary at 65 µm from the bottom of the central axons. This selection was thresholded, binarized, and the number of objects it contains determined using the Analyze Particles function.

Hyperstacks of EB3-GFP images were assembled using FIJI (Schindelin et al., 2012) and segments of axons were traced for kymography using the segmented line tool. For peripheral axons, a segment was defined as an area of axon between two branch nodes, or between the first visible portion of axon and the first node of branching. Growth cones and filopodia were excluded from EB3-GFP analysis. For unbranched central axons, a segment was defined as the entire visible length of either the ascending or descending central axon within each field of view. Kymographs were made using the Multi Kymograph plugin (developed by J. Rietdorf and A. Seitz, European Molecular Biology Laboratory, 2004). Comet parameters were measured from the resulting kymographs. Comparisons between experimental conditions were made using the Mann-Whitney test for non-parametric data.

Adult Body Size Measurements

Zebrafish were raised for this experiment by in-crossing wildtype or *klc4*^{uw314} homozygous siblings. Larva were placed in 3L tanks side-by-side and subjected to the same light cycle and feeding schedule during rearing. At 7 weeks and 9 weeks, fish were briefly anesthetized with 0.02% tricaine, placed on white waterproof surface, measured with a ruler, and photographed.

Feeding Experiment

Feeding experiments were conducted as in Howe et al., 2018. Briefly, adult zebrafish were isolated in individual 1L tanks without food for 48 hours, then 50 larval zebrafish were added to each tank. The fish were allowed to feed on the larvae for one hour, then removed from the tank to allow counting of the remaining larvae. All tested animals were of AB background.

Novel Tank Diving Test

The evening before an experiment, fish were moved to the behavior experiment room and allowed to acclimate overnight. Exposure to novel tank was carried out in the morning, and the order of which genotype received exposure first was randomized. The novel tank had 3 opaque sides to block potential views of other fish and one clear side for imaging. The water in the novel tank was changed between groups. Fish were netted from their 3L home tank, released into the novel tank, and allowed to explore for 3 minutes before being removed and placed into a recovery tank. All tested animals were of AB background.

Habituation Experiment

Two weeks prior to an experiment, adults were sorted into separate 3L tanks with 5-6 individuals of the same genotype in each. Experiment was conducted in a similar manner as described above, but fish were allowed to explore for 10 minutes before removal. Novel tank exposure was repeated on the same groups twice a week for 3 weeks. Exposures were conducted a minimum of two days apart. The experiment was repeated for another 3 weeks with an additional two groups of 6 fish per genotype. All tested animals were of AB background. When possible, groups were divided into similar ratios of male and female fish for a total of 11 females and 12 males within each genotype. The group compositions were as follows: **wild type**: group 1 (3 females [F], 2 males [M]) group 2, (3 F, 3 M), group 3 (3 F, 3 M), group 4 (2 F, 4 M), ***klc4***^{uw314}: group 1 (2 F, 3 M), group 2, (3 F, 3 M), group 3 (3 F, 3 M), group 4 (3 F, 3 M).

666
667 **Automated Tracking of Adults**
668 For the habituation experiment, automated tracking of zebrafish through ToxTrac (Rodriguez et al.,
669 2018) was used to quantify swim velocity and percent of time spent in the upper zone. When
670 necessary for accurate tracking, background subtraction was performed on movies prior to using
671 ToxTrac. This was accomplished by subtracting the first frame of each movie (showing only the empty
672 tank) from subsequent frames in the movie via FIJI (Schindelin et al., 2012). Operations were
673 performed using Clij2 where possible to speed up processing time (Haase et al., 2019).
674
675 **Statistics**
676 Statistical analyses and graphs were generated with Graphpad Prism. See figure legends for details on
677 sample sizes, specific statistical tests used, error bars and p values). Data were checked for normality
678 before deciding on a statistical test. Plots using 95% confidence intervals (CI) were considered to be
679 significant when the 95% CI ranges did not overlap.
680
681 **Acknowledgements**
682 The authors would like to thank the members of the Huisken lab for technical expertise and
683 intellectual contributions, particularly Kurt Weiss, Joe Li, and Alyssa Graves. We are grateful to Katie
684 Drerup and Bill Bement for critical reading and feedback on this manuscript, which greatly improved
685 the final work. We also give our heartfelt thanks to the current and former members of the Halloran
686 lab for their support of and contributions to this work, especially Conlin Bass for valuable work during
687 the initial characterization of *klc4* expression pattern, and Daniel North for fish care and maintenance.
688
689 **Funding**
690
691 This work was supported by funds to Mary Halloran from the National Institutes of Health (R01
692 NS086934, R21 NS116326) and funds to Elizabeth Haynes from the National Institutes of Health (F32
693 NS098689). The Morgridge Institute for Research provided support for the Huisken lab and the light
694 sheet microscope.
695
696
697 **Ethics Statement**
698 This study was performed in accordance with the recommendations in the Guide for the Care and Use
699 of Laboratory Animals of the National Institutes of Health. Animals were handled according to
700 approved institutional animal care and use committee protocols of the University of Wisconsin.
701
702 **Competing interests**

703 K. Eliceiri is a consultant for Bruker, the manufacturer of the Opterra Swept Field Confocal microscope
704 used in this work.

705

706 **References**
707 Andersen, E., N. Asuri, and M. Halloran. 2011. In vivo imaging of cell behaviors and F-actin
708 reveals LIM-HD transcription factor regulation of peripheral versus central sensory axon
709 development. *Neural Dev*. 6:27.

710 Andersen, E.F., and M.C. Halloran. 2012. Centrosome movements in vivo correlate with specific
711 neurite formation downstream of LIM homeodomain transcription factor activity.
712 *Development*. 139:3590-3599.
713 Anton, Z., et al. . 2021. Molecular mechanisms for kinesin-1 direct membrane recognition.
714 *bioRxiv*. 2021.01.20.427326.
715 Armijo-Weingart, L., and G. Gallo. 2017. It takes a village to raise a branch: Cellular mechanisms
716 of the initiation of axon collateral branches. *Molecular and Cellular Neuroscience*. 84:36-
717 47.
718 Baek, J.H., J. Lee, H.S. Yun, C.W. Lee, J.Y. Song, H.D. Um, J.K. Park, I.C. Park, J.S. Kim, E.H. Kim,
719 and S.G. Hwang. 2018. Kinesin light chain-4 depletion induces apoptosis of
720 radioresistant cancer cells by mitochondrial dysfunction via calcium ion influx. *Cell*
721 *Death Dis*. 9:496.
722 Bayrakli, F., H.G. Poyrazoglu, S. Yuksel, C. Yakicier, B. Erguner, M.S. Sagiroglu, B. Yuceturk, B.
723 Ozer, S. Doganay, B. Tanrikulu, A. Seker, F. Akbulut, A. Ozen, H. Per, S. Kumandas, Y.
724 Altuner Torun, Y. Bayri, M. Sakar, A. Dagcinar, and I. Ziyal. 2015. Hereditary spastic
725 paraplegia with recessive trait caused by mutation in KLC4 gene. *J Hum Genet*. 60:763-
726 768.
727 Bazvand, F., M. Keramatipour, H. Riazi-Esfahani, and A. Mahmoudi. 2021. SPOAN syndrome: a
728 novel mutation and new ocular findings; a case report. *BMC Neurology*. 21:24.
729 Cai, D., A.D. Hoppe, J.A. Swanson, and K.J. Verhey. 2007. Kinesin-1 structural organization and
730 conformational changes revealed by FRET stoichiometry in live cells. *Journal of Cell*
731 *Biology*. 176:51-63.
732 Chen, W.V., C.L. Nwakeze, C.A. Denny, S. O'Keeffe, M.A. Rieger, G. Mountoufaris, A. Kirner, J.D.
733 Dougherty, R. Hen, Q. Wu, and T. Maniatis. 2017. Pcdhαc2 is required for axonal tiling
734 and assembly of serotonergic circuitries in mice. *Science*. 356:406-411.
735 Chiba, K., K.M. Ori-McKenney, S. Niwa, and R.J. McKenney. 2021. Reconstitution of Kinesin-1
736 Activation. *bioRxiv*:2021.2003.2012.434960.
737 Choi, J.-H., Y.-M. Jeong, S. Kim, B. Lee, K. Ariyasiri, H.-T. Kim, S.-H. Jung, K.-S. Hwang, T.-I. Choi,
738 C.O. Park, W.-K. Huh, M. Carl, J.A. Rosenfeld, S. Raskin, A. Ma, J. Gecz, H.-G. Kim, J.-S.
739 Kim, H.-C. Shin, D.-S. Park, R. Gerlai, B.B. Jamieson, J.S. Kim, K.J. Iremonger, S.H. Lee, H.-
740 S. Shin, and C.-H. Kim. 2018. Targeted knockout of a chemokine-like gene increases
741 anxiety and fear responses. *Proceedings of the National Academy of Sciences*.
742 115:E1041.
743 Cockburn, J.J.B., S.J. Hesketh, P. Mulhair, M. Thomsen, M.J. O'Connell, and M. Way. 2018.
744 Insights into Kinesin-1 Activation from the Crystal Structure of KLC2 Bound to JIP3.
745 *Structure*. 26:1486-1498 e1486.
746 Courchet, J., T.L. Lewis, Jr., S. Lee, V. Courchet, D.Y. Liou, S. Aizawa, and F. Polleux. 2013.
747 Terminal axon branching is regulated by the LKB1-NUAK1 kinase pathway via
748 presynaptic mitochondrial capture. *Cell*. 153:1510-1525.
749 Csordas, G., D. Weaver, and G. Hajnoczky. 2018. Endoplasmic Reticulum-Mitochondrial
750 Contactology: Structure and Signaling Functions. *Trends in cell biology*. 28:523-540.
751 Dent, E.W., and K. Kalil. 2001. Axon branching requires interactions between dynamic
752 microtubules and actin filaments. *J Neurosci*. 21:9757-9769.

753 Du, J., Y. Wei, L. Liu, Y. Wang, R. Khairova, R. Blumenthal, T. Tragon, J.G. Hunsberger, R.
754 Machado-Vieira, W. Drevets, Y.T. Wang, and H.K. Manji. 2010. A kinesin signaling
755 complex mediates the ability of GSK-3beta to affect mood-associated behaviors. *Proc*
756 *Natl Acad Sci U S A*. 107:11573-11578.
757 Gallo, G. 2011. The cytoskeletal and signaling mechanisms of axon collateral branching.
758 *Developmental neurobiology*. 71:201-220.
759 Gibson, D.A., S. Tymanskyj, R.C. Yuan, H.C. Leung, J.L. Lefebvre, J.R. Sanes, A. Chédotal, and L.
760 Ma. 2014. Dendrite self-avoidance requires cell-autonomous slit/robo signaling in
761 cerebellar purkinje cells. *Neuron*. 81:1040-1056.
762 Gindhart, J.G., Jr., C.J. Desai, S. Beushausen, K. Zinn, and L.S. Goldstein. 1998. Kinesin light
763 chains are essential for axonal transport in Drosophila. *J Cell Biol*. 141:443-454.
764 Grueber, W.B., and A. Sagasti. 2010. Self-avoidance and Tiling: Mechanisms of Dendrite and
765 Axon Spacing. *Cold Spring Harbor Perspectives in Biology*. 2.
766 Gupta, S.K., K.F. Meiri, K. Mahfooz, U. Bharti, and S. Mani. 2010. Coordination between Extrinsic
767 Extracellular Matrix Cues and Intrinsic Responses to Orient the Centrosome in Polarizing
768 Cerebellar Granule Neurons. *The Journal of Neuroscience*. 30:2755.
769 Haase, R., L.A. Royer, P. Steinbach, D. Schmidt, A. Dibrov, U. Schmidt, M. Weigert, N. Maghelli,
770 P. Tomancak, F. Jug, and E.W. Myers. 2019. CLIJ: GPU-accelerated image processing for
771 everyone. *Nature Methods*. 17:5-6.
772 Hakeda-Suzuki, S., S. Berger-Müller, T. Tomasi, T. Usui, S.-y. Horiuchi, T. Uemura, and T. Suzuki.
773 2011. Golden Goal collaborates with Flamingo in conferring synaptic-layer specificity in
774 the visual system. *Nature Neuroscience*. 14:314-323.
775 Halloran, M.C., S.M. Severance, C.S. Yee, D.L. Gemza, J.A. Raper, and J.Y. Kuwada. 1999.
776 Analysis of a zebrafish semaphorin reveals potential functions in vivo. *Developmental*
777 *Dynamics*. 214:13-25.
778 Hirokawa, N., S. Niwa, and Y. Tanaka. 2010. Molecular motors in neurons: transport
779 mechanisms and roles in brain function, development, and disease. *Neuron*. 68:610-638.
780 Howe, H.B., P.B. McIntyre, and M.A. Wolman. 2018. Adult zebrafish primarily use vision to
781 guide piscivorous foraging behavior | Elsevier Enhanced Reader. *Behavioural Processes*.
782 157:230-237.
783 Jiang, M., J. Esteve-Rudd, V.S. Lopes, T. Diemer, C. Lillo, A. Rump, and D.S. Williams. 2015.
784 Microtubule motors transport phagosomes in the RPE, and lack of KLC1 leads to AMD-
785 like pathogenesis. *J Cell Biol*. 210:595-611.
786 Kalil, K., and E.W. Dent. 2014. Branch management: mechanisms of axon branching in the
787 developing vertebrate CNS. *Nat Rev Neurosci*. 15:7-18.
788 Kamal, A., G.B. Stokin, Z. Yang, C.H. Xia, and L.S. Goldstein. 2000. Axonal transport of amyloid
789 precursor protein is mediated by direct binding to the kinesin light chain subunit of
790 kinesin-I. *Neuron*. 28:449-459.
791 Katori, S., Y. Noguchi-Katori, A. Okayama, Y. Kawamura, W. Luo, K. Sakimura, T. Hirabayashi, T.
792 Iwasato, and T. Yagi. 2017. Protocadherin-αC2 is required for diffuse projections of
793 serotonergic axons. *Scientific Reports*. 7:15908.
794 Ketschek, A., S. Jones, M. Spillane, F. Korobova, T. Svitkina, and G. Gallo. 2015. Nerve growth
795 factor promotes reorganization of the axonal microtubule array at sites of axon
796 collateral branching. *Dev Neurobiol*. 75:1441-1461.

797 Khan, K.M., A.D. Collier, D.A. Meshalkina, E.V. Kysil, S.L. Khatsko, T. Kolesnikova, Y.Y. Morzherin,
798 J.E. Warnick, A.V. Kalueff, and D.J. Echevarria. 2017. Zebrafish models in
799 neuropsychopharmacology and CNS drug discovery. *Br J Pharmacol*. 174:1925-1944.
800 Kimmel, C.B., W.W. Ballard, S.R. Kimmel, B. Ullmann, and T.F. Schilling. 1995. Stages of
801 embryonic development of the zebrafish. *Dev Dyn*. 203:253-310.
802 Knafo, S., K. Fidelin, A. Prendergast, P.-E.B. Tseng, A. Parrin, C. Dickey, U.L. Böhm, S.N.
803 Figueiredo, O. Thouvenin, H. Pascal-Moussellard, and C. Wyart. 2017. Mechanosensory
804 neurons control the timing of spinal microcircuit selection during locomotion.
805 Krols, M., G. Bultynck, and S. Janssens. 2016. ER-Mitochondria contact sites: A new regulator of
806 cellular calcium flux comes into play. *J Cell Biol*. 214:367-370.
807 Kwan, K.M., E. Fujimoto, C. Grabher, B.D. Mangum, M.E. Hardy, D.S. Campbell, J.M. Parant, H.J.
808 Yost, J.P. Kanki, and C.B. Chien. 2007. The Tol2kit: a multisite gateway-based
809 construction kit for Tol2 transposon transgenesis constructs. *Dev Dyn*. 236:3088-3099.
810 Lee, T.J., J.W. Lee, E.M. Haynes, K.W. Eliceiri, and M.C. Halloran. 2017. The Kinesin Adaptor
811 Calsyntenin-1 Organizes Microtubule Polarity and Regulates Dynamics during Sensory
812 Axon Arbor Development. *Front Cell Neurosci*. 11:107.
813 Liu, Y., and M.C. Halloran. 2005. Central and peripheral axon branches from one neuron are
814 guided differentially by Semaphorin3D and transient axonal glycoprotein-1. *J Neurosci*.
815 25:10556-10563.
816 Lu, W., and V.I. Gelfand. 2017. Moonlighting Motors: Kinesin, Dynein, and Cell Polarity. *Trends*
817 *Cell Biol*. 27:505-514.
818 Matthews, B.J., M.E. Kim, J.J. Flanagan, D. Hattori, J.C. Clemens, S.L. Zipursky, and W.B.
819 Grueber. 2007. Dendrite Self-Avoidance Is Controlled by Dscam. *Cell*. 129:593-604.
820 Maximino, C., T.M. de Brito, A.W. da Silva Batista, A.M. Herculano, S. Morato, and A. Gouveia.
821 2010. Measuring anxiety in zebrafish: A critical review. *Behavioural Brain Research*.
822 214:157-171.
823 Melo, U.S., L.I. Macedo-Souza, T. Figueiredo, A.R. Muotri, J.G. Gleeson, G. Coux, P. Armas, N.B.
824 Calcaterra, J.P. Kitajima, S. Amorim, T.R. Olavio, K. Griesi-Oliveira, G.C. Coatti, C.R.
825 Rocha, M. Martins-Pinheiro, C.F. Menck, M.S. Zaki, F. Kok, M. Zatz, and S. Santos. 2015.
826 Overexpression of KLC2 due to a homozygous deletion in the non-coding region causes
827 SPOAN syndrome. *Hum Mol Genet*. 24:6877-6885.
828 Millard, S.S., J.J. Flanagan, K.S. Pappu, W. Wu, and S.L. Zipursky. 2007. Dscam2 mediates axonal
829 tiling in the Drosophila visual system. *Nature*. 447:720-724.
830 Mochizuki, H., H. Toda, M. Ando, M. Kurusu, T. Tomoda, and K. Furukubo-Tokunaga. 2011. Unc-
831 51/ATG1 controls axonal and dendritic development via kinesin-mediated vesicle
832 transport in the Drosophila brain. *PLoS One*. 6:e19632.
833 Morfini, G., N. Schmidt, C. Weissmann, G. Pigino, and S. Kins. 2016. Conventional kinesin:
834 Biochemical heterogeneity and functional implications in health and disease. *Brain Res*
835 *Bull*. 126:347-353.
836 Navone, F., J. Niclas, N. Hom-Booher, L. Sparks, H.D. Bernstein, G. McCaffrey, and R.D. Vale.
837 1992. Cloning and expression of a human kinesin heavy chain gene: interaction of the
838 COOH-terminal domain with cytoplasmic microtubules in transfected CV-1 cells. *Journal*
839 *of Cell Biology*. 117:1263-1275.

840 Orefice, L.L., A.L. Zimmerman, A.M. Chirila, S.J. Sleboda, J.P. Head, and D.D. Ginty. 2016.
841 Peripheral Mechanosensory Neuron Dysfunction Underlies Tactile and Behavioral
842 Deficits in Mouse Models of ASDs. *Cell*. 166:299-313.
843 Pernigo, S., M.S. Chegkazi, Y.Y. Yip, C. Treacy, G. Glorani, K. Hansen, A. Politis, S. Bui, M.P.
844 Dodding, and R.A. Steiner. 2018. Structural basis for isoform-specific kinesin-1
845 recognition of Y-acidic cargo adaptors. *Elife*. 7.
846 Ponomareva, O.Y., K.W. Eliceiri, and M.C. Halloran. 2016. Charcot-Marie-Tooth 2b associated
847 Rab7 mutations cause axon growth and guidance defects during vertebrate sensory
848 neuron development. *Neural Dev*. 11:2.
849 Ponomareva, O.Y., I.C. Holmen, A.J. Sperry, K.W. Eliceiri, and M.C. Halloran. 2014. Calsyntenin-1
850 regulates axon branching and endosomal trafficking during sensory neuron
851 development in vivo. *The Journal of neuroscience : the official journal of the Society for*
852 *Neuroscience*. 34:9235-9248.
853 Qiang, L., W. Yu, M. Liu, J.M. Solowska, and P.W. Baas. 2010. Basic fibroblast growth factor
854 elicits formation of interstitial axonal branches via enhanced severing of microtubules.
855 *Mol Biol Cell*. 21:334-344.
856 Rahman, A., A. Kamal, E.A. Roberts, and L.S. Goldstein. 1999. Defective kinesin heavy chain
857 behavior in mouse kinesin light chain mutants. *J Cell Biol*. 146:1277-1288.
858 Randall, T.S., Y.Y. Yip, D.J. Wallock-Richards, K. Pfisterer, A. Sanger, W. Ficek, R.A. Steiner, A.J.
859 Beavil, M. Parsons, and M.P. Dodding. 2017. A small-molecule activator of kinesin-1
860 drives remodeling of the microtubule network.
861 Randlett, O., L. Poggi, Flavio R. Zolessi, and William A. Harris. 2011. *Neuron*. 70:266-280.
862 Rezakhaniha, R., A. Agianniotis, J.T.C. Schrauwen, A. Griffa, D. Sage, C.V.C. Bouten, F.N.v.d.
863 Vosse, M. Unser, and N. Stergiopulos. 2011. Experimental investigation of collagen
864 waviness and orientation in the arterial adventitia using confocal laser scanning
865 microscopy. *Biomechanics and Modeling in Mechanobiology*. 11:461-473.
866 Rodriguez, A., H. Zhang, J. Klaminder, T. Brodin, P.L. Andersson, and M. Andersson. 2018.
867 ToxTrac: A fast and robust software for tracking organisms. *Methods in Ecology and*
868 *Evolution*. 9:460-464.
869 Rowland, A.A., and G.K. Voeltz. 2012. Endoplasmic reticulum-mitochondria contacts: function
870 of the junction. *Nature reviews*. 13:607-625.
871 Saez, T.M.M., I. Fernandez Bessone, M.S. Rodriguez, M. Alloatti, M.G. Otero, L.E. Cromberg,
872 V.M. Pozo Devoto, G. Oubina, L. Sosa, M.G. Buffone, D.M. Gelman, and T.L. Falzone.
873 2020. Kinesin-1-mediated axonal transport of CB1 receptors is required for cannabinoid-
874 dependent axonal growth and guidance. *Development*. 147.
875 Sagasti, A., M.R. Guido, D.W. Raible, and A.F. Schier. 2005. Repulsive interactions shape the
876 morphologies and functional arrangement of zebrafish peripheral sensory arbors. *Curr*
877 *Biol*. 15:804-814.
878 Schindelin, J., I. Arganda-Carreras, E. Frise, V. Kaynig, M. Longair, T. Pietzsch, S. Preibisch, C.
879 Rueden, S. Saalfeld, B. Schmid, J.-Y. Tinevez, D.J. White, V. Hartenstein, K. Eliceiri, P.
880 Tomancak, and A. Cardona. 2012. Fiji: an open-source platform for biological-image
881 analysis. *Nature Methods*. 9:676-682.
882 Seeger, M.A., and S.E. Rice. 2010. Microtubule-associated Protein-like Binding of the Kinesin-1
883 Tail to Microtubules. *Journal of Biological Chemistry*. 285:8155-8162.

884 Senti, K.-A., T. Usui, K. Boucke, U. Greber, T. Uemura, and B.J. Dickson. 2003. Flamingo
885 Regulates R8 Axon-Axon and Axon-Target Interactions in the Drosophila Visual System.
886 *Current Biology*. 13:828-832.
887 Shah, A.N., C.F. Davey, A.C. Whitebirch, A.C. Miller, and C.B. Moens. 2015. Rapid reverse
888 genetic screening using CRISPR in zebrafish. *Nature Methods*. 12:535-540.
889 Shima, T., M. Morikawa, J. Kaneshiro, T. Kambara, S. Kamimura, T. Yagi, H. Iwamoto, S. Uemura,
890 H. Shigematsu, M. Shirouzu, T. Ichimura, T.M. Watanabe, R. Nitta, Y. Okada, and N.
891 Hirokawa. 2018. Kinesin-binding–triggered conformation switching of microtubules
892 contributes to polarized transport. *Journal of Cell Biology*. 217:4164-4183.
893 Smith, C.J., J.D. Watson, M.K. VanHoven, D.A. Colón-Ramos, and D.M. Miller. 2012. Netrin
894 (UNC-6) mediates dendritic self-avoidance. *Nature Neuroscience*. 15:731-737.
895 Soba, P., S. Zhu, K. Emoto, S. Younger, S.-J. Yang, H.-H. Yu, T. Lee, L.Y. Jan, and Y.-N. Jan. 2007.
896 Drosophila Sensory Neurons Require Dscam for Dendritic Self-Avoidance and Proper
897 Dendritic Field Organization. *Neuron*. 54:403-416.
898 Spead, O., and F.E. Poulain. 2020. Trans-Axonal Signaling in Neural Circuit Wiring. *International*
899 *Journal of Molecular Sciences*. 21.
900 Spillane, M., A. Ketschek, T.T. Merianda, J.L. Twiss, and G. Gallo. 2013. Mitochondria coordinate
901 sites of axon branching through localized intra-axonal protein synthesis. *Cell Rep*.
902 5:1564-1575.
903 Stepanova, T., J. Slemmer, C.C. Hoogenraad, G. Lansbergen, B. Dortland, C.I. De Zeeuw, F.
904 Grosveld, G. van Cappellen, A. Akhmanova, and N. Galjart. 2003. Visualization of
905 microtubule growth in cultured neurons via the use of EB3-GFP (end-binding protein 3-
906 green fluorescent protein). *J Neurosci*. 23:2655-2664.
907 Tao, K., N. Matsuki, and R. Koyama. 2014. AMP-activated protein kinase mediates activity-
908 dependent axon branching by recruiting mitochondria to axon. *Developmental*
909 *neurobiology*. 74:557-573.
910 Tomasi, T., S. Hakeda-Suzuki, S. Ohler, A. Schleiffer, and T. Suzuki. 2008. The Transmembrane
911 Protein Golden Goal Regulates R8 Photoreceptor Axon-Axon and Axon-Target
912 Interactions. *Neuron*. 57:691-704.
913 Triclin, S., D. Inoue, J. Gaillard, Z.M. Htet, M.E. DeSantis, D. Portran, E. Derivery, C. Aumeier, L.
914 Schaedel, K. John, C. Leterrier, S.L. Reck-Peterson, L. Blanchoin, and M. Théry. 2021.
915 Self-repair protects microtubules from destruction by molecular motors. *Nature*
916 *Materials*. 20:883-891.
917 Williams, K., and A.B. Ribera. 2020. Long-lived zebrafish Rohon-Beard cells. *Developmental*
918 *Biology*. 464:45-52.
919 Winkle, C.C., K.L. Taylor, E.W. Dent, G. Gallo, K.F. Greif, and S.L. Gupton. 2016. Beyond the
920 cytoskeleton: The emerging role of organelles and membrane remodeling in the
921 regulation of axon collateral branches. *Developmental neurobiology*. 76:1293-1307.
922 Wong, H.H., J.Q. Lin, F. Strohl, C.G. Roque, J.M. Cioni, R. Cagnetta, B. Turner-Bridger, R.F. Laine,
923 W.A. Harris, C.F. Kaminski, and C.E. Holt. 2017. RNA Docking and Local Translation
924 Regulate Site-Specific Axon Remodeling In Vivo. *Neuron*. 95:852-868 e858.
925 Wong, K., M. Elegante, B. Bartels, S. Elkhayat, D. Tien, S. Roy, J. Goodspeed, C. Suciu, J. Tan, C.
926 Grimes, A. Chung, M. Rosenberg, S. Gaikwad, A. Denmark, A. Jackson, F. Kadri, K.M.
927 Chung, A. Stewart, T. Gilder, E. Beeson, I. Zapolsky, N. Wu, J. Cachat, and A.V. Kalueff.

928 2010. Analyzing habituation responses to novelty in zebrafish (Danio rerio). *Behavioural*
929 *Brain Research*. 208:450-457.
930 Wong, Y.L., and S.E. Rice. 2010. Kinesin's light chains inhibit the head- and microtubule-binding
931 activity of its tail. *Proc Natl Acad Sci U S A*. 107:11781-11786.
932 Wozniak, M.J., and V.J. Allan. 2006. Cargo selection by specific kinesin light chain 1 isoforms.
933 *EMBO J*. 25:5457-5468.
934 Yu, W., F.J. Ahmad, and P.W. Baas. 1994. Microtubule fragmentation and partitioning in the
935 axon during collateral branch formation. *J Neurosci*. 14:5872-5884.
936 Yu, W., L. Qiang, J.M. Solowska, A. Karabay, S. Korulu, and P.W. Baas. 2008. The microtubule-
937 severing proteins spastin and katanin participate differently in the formation of axonal
938 branches. *Mol Biol Cell*. 19:1485-1498.
939 Zhu, H., H.Y. Lee, Y. Tong, B.S. Hong, K.P. Kim, Y. Shen, K.J. Lim, F. Mackenzie, W. Tempel, and
940 H.W. Park. 2012. Crystal structures of the tetratricopeptide repeat domains of kinesin
941 light chains: insight into cargo recognition mechanisms. *PLoS One*. 7:e33943.
942 Ziv, L., A. Muto, P.J. Schoonheim, S.H. Meijsing, D. Strasser, H.A. Ingraham, M.J. Schaaf, K.R.
943 Yamamoto, and H. Baier. 2013. An affective disorder in zebrafish with mutation of the
944 glucocorticoid receptor. *Mol Psychiatry*. 18:681-691.

945

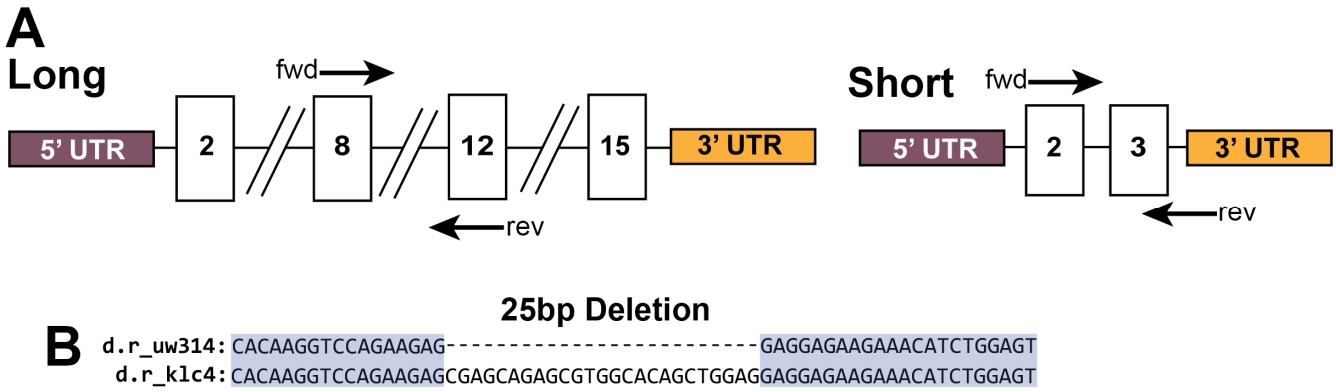

Figure 1 -- Supplemental Figure 1. A) Diagram of the primer design for the RT-PCR of the long and short isoforms of *klc4*. For the long isoform, the primers were designed for regions of exon 8 (fwd) and exon 12 (rev), which are not contained in the short isoform. The amplified product is 421 bp. For the short isoform, the primers were designed against exon 2 (contained in long isoform) and the short isoform 3'UTR (not contained in long isoform). The amplified product is 523 bp.**B)** The sequence alignment around the 25 bp deletion within exon 3 contained in *klc4*^{uw314} mutants.

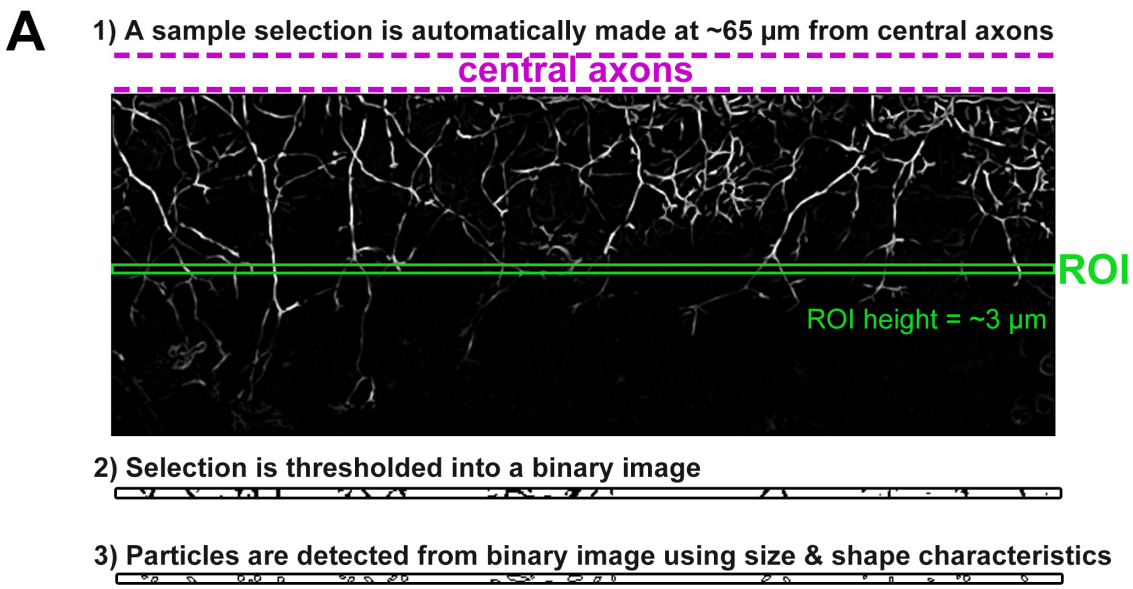

Figure 2 -- Supplemental Figure 2. Schematic describing our branch analysis method. A standard sized ROI (ROI_1) from the trunk over the yolk tube extension is selected with the top of the ROI_1 aligned to the bottom of the central axon fascicle. A second 3 µm ROI (green, ROI_2) is selected at the midpoint (~65 µm below the central axons) of ROI_1. ROI_2 is duplicated and then thresholded into a binary image. This binary image is run through Particle Analysis in ImageJ, which counts the number of particles present with gating for size and shape characteristics. We use the number of particles counted to represent the number of branches passing through ROI_2.

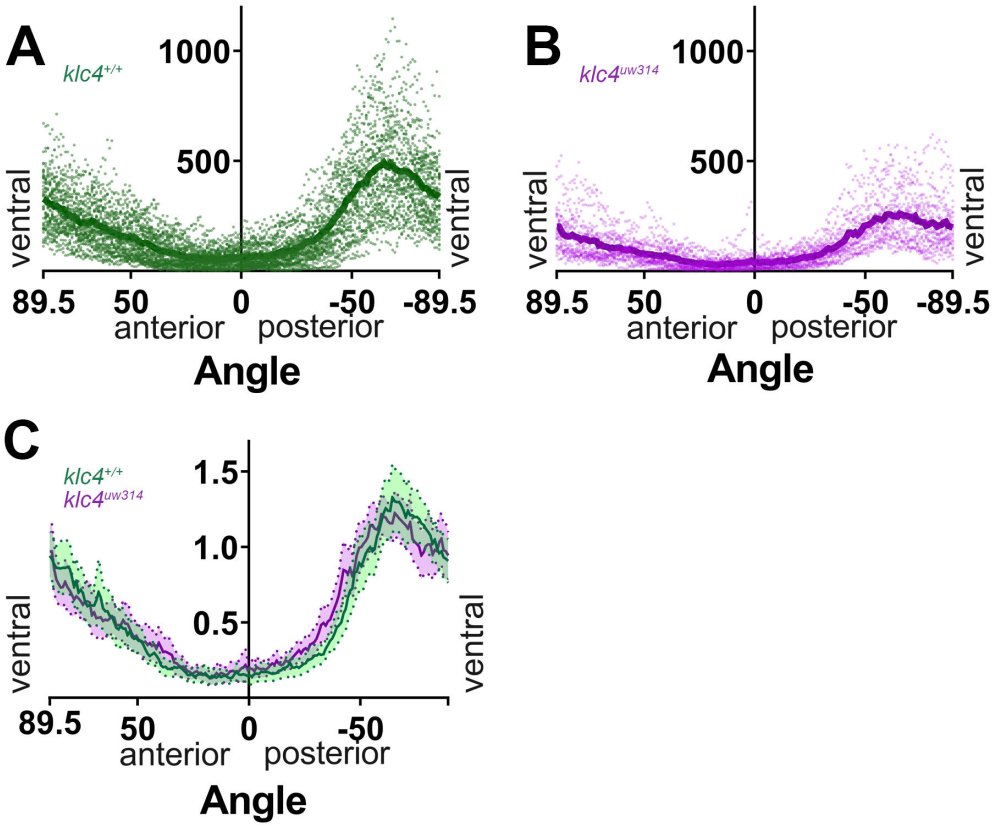

Figure 4 -- Supplemental Figure 4. Additional data for branch directionality profiling. **A)** All individual data points for the 40 wild type embryos analyzed (dots), with the mean overlayed (dark green line). **B)** All individual data points for the 23 *klc4*^{uw314} mutant embryos analyzed (dots), with the mean overlayed (magenta line). **C)** Axon directionality data normalized to total signal with posterior and anterior data displayed. Error bars = 95% CI.

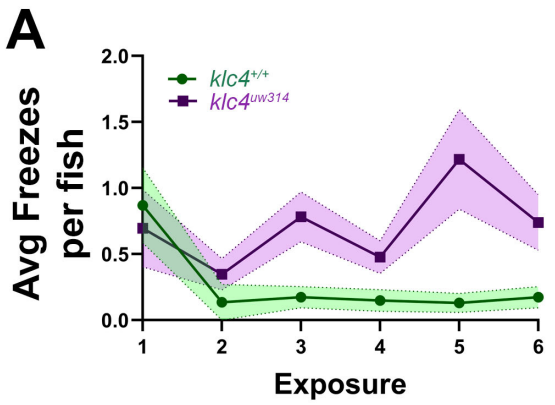

B

Exp	*Klc4*$^{+/+}$ (froze/total)	*Klc4*^{uw314} (froze/total)
1	7/23	8/23
2	1/23	7/23
3	4/23	11/23
4	3/20*	10/23
5	3/23	11/23
6	3/23	12/23

Figure 10 -- Supplemental Figure 10. Additional data for novel tank habituation experiments. **A)** The average number of freezing bouts per fish over the course of 6 exposures. **B)** The number of fish that froze out of the total number of fish in the experiment. * indicates data for 3 fish lost from one exposure due to video equipment malfunction. These data could not be generated again since fish had already been exposed to the tank, so the group N for this exposure is 20 instead of 23.